Elucidating efficiency losses in cuprous oxide (Cu_2O) photovoltaics and identifying strategies for efficiency improvement

by

Riley Eric Brandt

B.S., Mechanical Engineering
Massachusetts Institute of Technology (2011)

Submitted to the Department of Mechanical Engineering
in partial fulfillment of the requirements for the degree of

Master of Science in Mechanical Engineering

at the

MASSACHUSETTS INSTITUTE OF TECHNOLOGY

June 2013

Author .....
Department of Mechanical Engineering
May 10, 2013

Certified by .....
Tonio Buonassisi
Associate Professor of Mechanical Engineering
Thesis Supervisor

Accepted by .....
David Hardt, Professor of Mechanical Engineering
Chairman, Department Committee on Graduate Theses

Elucidating efficiency losses in cuprous oxide (Cu_2O) photovoltaics and identifying strategies for efficiency improvement

by

Riley Eric Brandt

Submitted to the Department of Mechanical Engineering
on May 10, 2013, in partial fulfillment of the
requirements for the degree of
Master of Science in Mechanical Engineering

Abstract

In this thesis, I fabricated and characterized a series of thin-film cuprous oxide (Cu_2O) photovoltaic devices. I constructed several different device designs, using sputtered and electrochemically deposited Cu_2O. Characterization was done using XRD, SEM, optical spectroscopy, quantum efficiency, current-voltage, and capacitance-voltage measurements. Then, these devices were modeled using SCAPS-1D, a numerical simulation package, as well as MATLAB for analytical solutions. This simulation enabled a quantitative breakdown of efficiency losses in Cu_2O devices. Simulations suggest that low device efficiencies of 0.3-0.6% may be explained in part by poor bulk transport properties in the Cu_2O. However, the predominant efficiency loss comes from an unoptimized *p-n* heterojunction, in which a large negative conduction band offset and structural defects lead to a low built-in voltage and high recombination activity. The effects of interface engineering are demonstrated in experiment and simulation. Broader simulations suggest opportunities for future efficiency improvements towards 10%. These include the improvement of bulk properties, the selection of alternative pairing materials, novel device structures, and the possibility of multijunction cells.

Thesis Supervisor: Tonio Buonassisi
Title: Associate Professor of Mechanical Engineering

Acknowledgments

Numerous individuals and organizations have offered intellectual, financial, and motivational support in the process of performing this research. Here, I would like to thank them all more than I could hope to in words.

The staff at the Harvard CNS and MIT EML, and especially Kurt Broderick, have directly taught me many of the fabrication skills used here, and for their patience and dedication I am very thankful. Many colleagues of mine have also been generous in donating their time and knowledge: Patrick Brown in the ONE lab, and Yun Seog Lee, Sin-Cheng Siah, Rupak Chakraborty, and Mark Winkler in the PV Lab.

All of the PV Lab members deserve an acknowledgement here, for all the things they've directly and indirectly taught me, for all of our conversations academic and otherwise, and for their motivational support in difficult times. In particular, I wish to acknowledge our advisor, Professor Tonio Buonassisi. Tonio has been tremendously generous in teaching, advising, and mentorship roles. He has helped provide focus for my scattered ideas, and has accommodated this young engineer's periods of doubt and self-reflection regarding career choices. I am very fortunate to work with the PV Lab team.

Beyond the lab, my source of balance and happiness, and somehow both motivation and distraction, are my close friends: Dan, Peter, Josh, Bill, Carmen, Maia, Emily, Mimi, and many others unnamed here. I hope that I may repay your kindness and support.

Financially, I have been extremely fortunate while pursuing my graduate school ambitions. Both the family of Walter A. Rosenblith, benefactors of the Presidential Graduate Fellowship, as well as the National Science Foundation Graduate Research Fellowship, have been incredible enablers of this work.

Lastly, and most importantly, I wish to thank my family. My grandparents, my parents Gary and Lori, and my siblings Taryn, Kaci, and Stirling, have all been immensely supportive. Their drive, their ingenuity, and their success, are constant inspirations. Thank you.

Contents

List of Figures

List of Tables

Chapter 1

Introduction

Throughout history, the world's primary energy sources have undergone several evolutions. Prior to the industrial revolution, energy came almost exclusively from biomass, as well as small hydro and wind-powered mills. With increasing demand for heat, then propulsion, and finally electricity, biomass became peat, then coal, then petroleum products such as kerosene and gasoline. The joules contained in these sources are all accumulated photon energy, captured and stored over millions of years by the organic matter of the earth. This energy would not exist without the sun's illumination.

The 21st century has the potential to be the century of solar power. The solar resource is tremendous; with an AM1.5 solar flux of 1000 W/m^2 providing 37,000 TW of peak power on the earth's landmass. Given our global power consumption of 15 TW, covering 1.4% of the earth's landmass with 15% efficient photovoltaic modules, operating at a 20% capacity factor, could supply the current world energy demand.

In 2012, annual solar deployment reached 30.9 GW_{peak}, a 12% growth over 2011 [2]. Worldwide, 250 GW_{peak} of solar capacity[1] would satisfy all new electricity demand. As these replacement levels are approached, the cost of producing a PV module continues to drop, helping to bring down the levelized cost of electricity for solar to become more grid-competitive.

This thesis, however, is not the story of PV, but that of a specific semiconductor, cuprous oxide (Cu_2O), and its prospects for fulfilling the role of a future photovoltaic

[1] Assuming 2 TW of demand growing at 2.3% per year; solar at a 20% capacity factor.

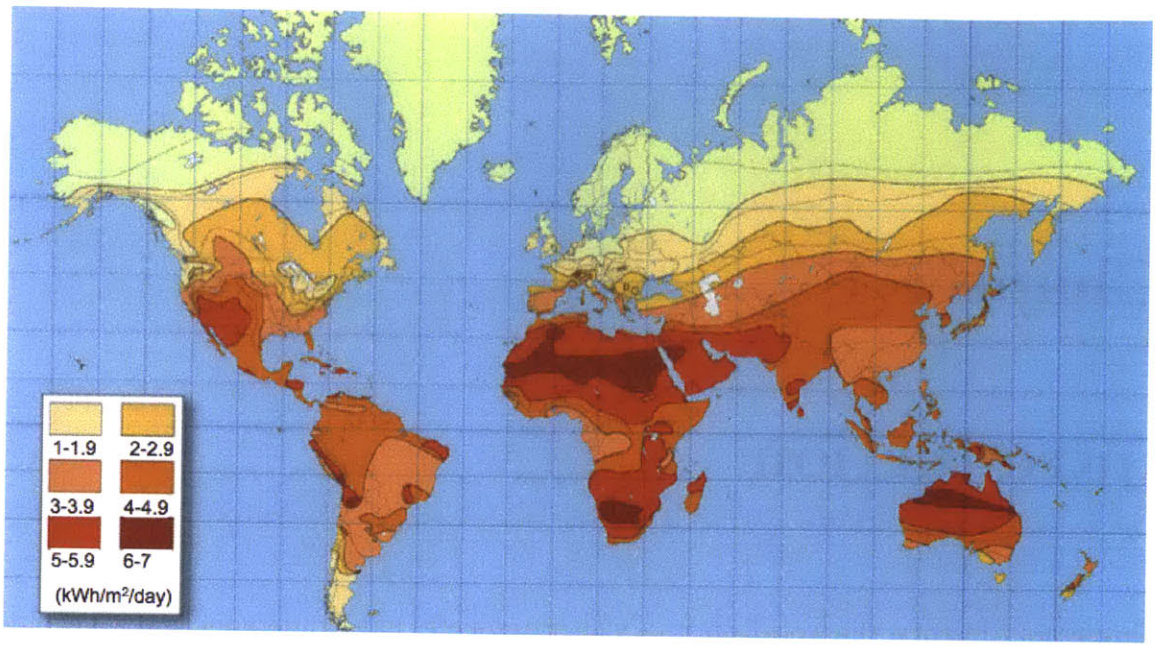

Figure 1-1: Average insolation worldwide in units of kWh/m^2/day [1]. Approximately 32 kWh/m^2/day are incident on the outer atmosphere, but losses in the atmosphere, the earth's rotation, and the projected area off-equator result in significantly less average insolation at the earth's surface.

material. The focus will be on explaining why Cu_2O photovoltaics have yet to achieve economical efficiency targets. Cu_2O devices were fabricated, characterized, and simulated, with the goal of prioritizing important scientific questions and charting a path for future efficiencies. The chapters of the present work will trace this journey from past, to present, to future.

In Chapter 2, the basic physics of a Cu_2O solar cell are described, as well as the tools used to simulate cell operation based on the underlying physics.

In Chapter 3, the fabrication procedures for forming Cu_2O PV cells are outlined, including materials and device processing.

In Chapter 4, fabricated devices are characterized through a variety of techniques, to extract key device parameters and build an accurate device simulation.

In Chapter 5, these results are used to simulate possible Cu_2O cell improvements, as well as the sensitivity of each parameter with respect to cell efficiency. This chapter will identify research priorities and describe strategies for achieving higher efficiencies.

First, however, we begin with the history of Cu_2O research.

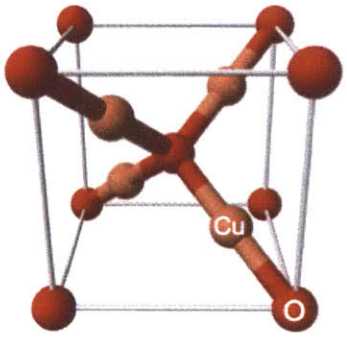

Figure 1-2: The cuprite lattice structure, unique to Cu_2O and Ag_2O, is cubic with fourfold coordinated oxygen. The lattice constant is $a = 4.2696$ Angstroms.

1.1 A History of Cu_2O

In 1839, Alexandre-Edmond Becquerel first observed the photovoltaic effect [3], when a silver chloride film dipped into an electrolyte produced a photocurrent. Further advances in photovoltaics would take nearly a century, predicated upon the discovery of the electron, the periodic table, and much of atomic and solid state physics. By the late 1800s it was known that oxidized copper showed light-sensitivity in its conductivity, along with selenium and stibnite (Sb_2S_3). The first formal investigation of this light sensitivity of Cu_2O occurred in 1916 on thermally oxidized copper foils [4]. Shortly thereafter in 1923, an electrochemical photovoltaic device was demonstrated with Cu_2O [5], and in 1926 Grondahl described a solid-state Cu/Cu_2O rectifier in terms that evoke fluidic metaphors for electrons [6]. Grondahl would continue to publish on this subject, and his work led to a proliferation of thin-film and thick foil Cu_2O devices as well as basic material characterization.

Cu_2O represents a compelling choice for a photovoltaic absorber material for several reasons: (a) its bandgap of 2.0 eV could achieve a Shockley-Queisser efficiency of 20%, and it could be implemented as the top cell in a multijunction stack; (b) its high absorption coefficient enables thin-film applications; (c) its non-toxicity and earth-abundance make it a candidate for low cost solar; and (d) it can be grown through a variety of techniques including sputtering, electrodeposition, and thermal oxidation [7]. Its unique cuprite lattice structure, shared only with Ag_2O, is cubic

and relatively sparsely packed like the zincblende lattice (see Fig. 1-2). The oxygen atoms are four-fold coordinated, while the copper are only two-fold.

By the 1980s, research on Cu_2O had accelerated dramatically, yet photovoltaic efficiencies remained low. The inability to dope Cu_2O *n*-type due to compensating copper vacancies [8] necessitated forming a Schottky junction or heterojunction. In 1986, Rakhshani reviewed several decades of device fabrication attempts, in which the record efficiency achieved was only 1.7% [9]. He concluded that in Schottky devices, it was most likely that reduction of Cu_2O to copper was limiting the Schottky barrier height to approximately 0.75 volts. Operating open-circuit voltages were even lower than this barrier height, and the conclusion was that a heterojunction might be the most viable strategy. The search for a heterojunction partner by Trivich in particular led to CdO, ZnO, and a variety of other *n*-type materials [9] [10]. Some of these materials, such as ZnSe, were found to react strongly at the heterojunction interface; only the oxides such as ZnO were demonstrated to be relatively stable.

In the intervening decades, discovery of new semiconductors rapidly accelerated, and their development began to advance beyond that of cuprous oxide. Cu_2S, $CuInSe_2$, Si, GaAs, CdTe, and InP saw improvements to 10% efficiencies and beyond by the 1980s. In the face of this development and the slow pace of Cu_2O cell efficiency improvements, research on Cu_2O subsided. It wasn't until 2006, when Mittiga *et al.* published a 2% efficient Cu_2O/ZnO cell, that research was reinvigorated [11].

Prior to this, much attention had been focused on improving the bulk Cu_2O absorber quality. In 2011, Minami *et al.* demonstrated that controlling the damage of heterojunction deposition at the interface could increase efficiency [12]. Minami's studies on minimizing interface damage with control of temperature and pulsed laser deposition (PLD) helped improve the efficiency to 3.83%. Further improvements by Nishi and Minami on control of ZnO PLD and the addition of Mg into ZnO in 2012 enabled a record efficiency of 4.1% [13] [14].

The primary question this thesis seeks to answer is why these conversion efficiencies remain low in Cu_2O cells, and especially thin-film cells. A scatterplot is shown in Figure 1-3 with the range of open-circuit voltage V_{OC} and short-circuit current

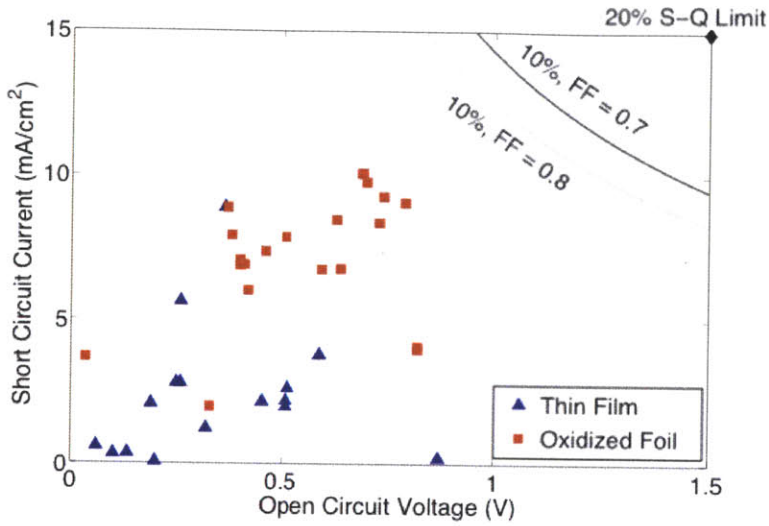

Figure 1-3: Scatterplot of V_{OC} and J_{SC} of Cu_2O cells, distinguishing between those produced by thermal foil oxidation [11][12][14][15][16], and those produced by thin-fim deposition [16][17][18]. The higher quality of oxidized devices is demonstrated, as well as the overall low voltages. Thresholds for 10% efficiency as well as the 20% Shockley-Queisser efficiency limit are presented.

J_{SC} values published in recent literature, separated by thin-film and thicker oxidized foil devices. It is clear that there are deficits in both V_{OC} and J_{SC}, especially in thin-film cells. The detailed-balance limits for these properties in an ideal device are plotted as well for reference: $V_{OC} = 1.5$ V and $J_{SC} = 15$ mA/cm^2.

The phenomena of an unusually low V_{OC} is not uncommon for thin-film heterojunctions. Many such devices perform below their detailed-balance V_{OC} limit. The nature of this deficit is not always well understood, and will be discussed further in Chapter 4. This discussion highlights the fact that lessons learned in the Cu_2O material system are highly applicable to other materials systems beyond Cu_2O. This connection represents the primary motivation for the present work.

1.2 Motivation and Goals

To re-emphasize, the slow progress of Cu_2O cell efficiencies is mirrored amongst many other candidate thin-film absorbers. There is a very apparent need for a stronger understanding of the nature of efficiency losses in Cu_2O and related solar cells.

To this end, the goal of this thesis is to fabricate a number of Cu_2O cells through

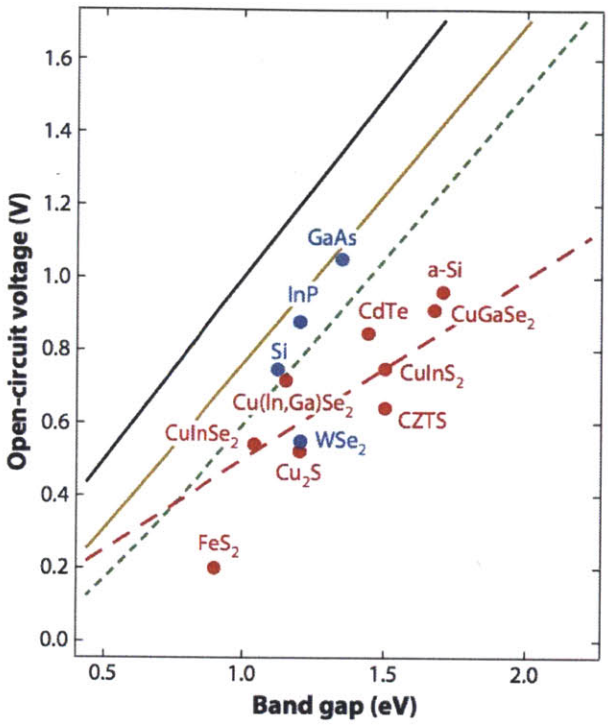

Figure 1-4: Low maximum V_{OC} in various cell types; many polycrystalline thin-film heterojunctions (red) exhibit voltages below their open-circuit voltage entitlement (green or yellow). Figure reproduced from Ref. [19].

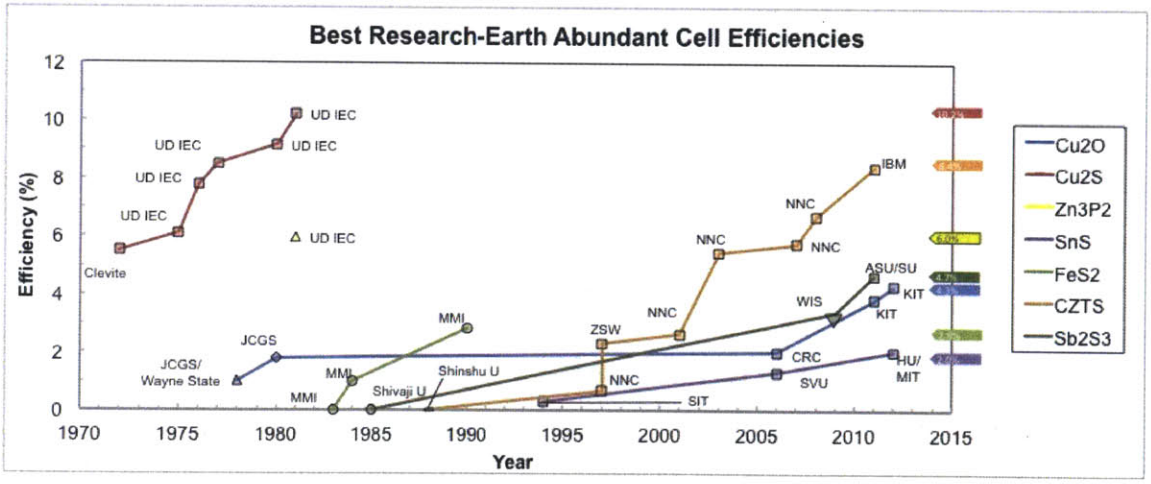

Figure 1-5: Efficiency vs. time plot of record performing devices, fabricated with different earth-abundant absorber materials and different geometries (prepared for forthcoming publication).

two different techniques, and in different device structures. These cells are then characterized through a variety of optical and electronic measurement techniques. These cell structures are modeled numerically and analytically to simulate their performance.

This modeling will allow for a breakdown of the specific efficiency losses in cuprous oxide photovoltaics. The models will then be used to identify routes to efficiency improvement, in the hopes of focusing the most important research questions and advancing efficiencies more rapidly in the future.

Chapter 2

Modeling and Simulating Cu_2O Cell Physics

As the fabrication of thin-film photovoltaics has yielded more complex device structures and higher efficiencies, the research community has developed correspondingly sophisticated theory. Today, differential equations to model the drift and diffusion of carriers in semiconductors are well understood. For well-behaved systems, in which simplifying assumptions may be made, these equations reduce to analytical expressions (Appendix A). Where numerical solutions are required, a range of computational tools have been developed to provide more accurate electronic transport models. These include PC-1D commonly used for crystalline-Si PV [20]; AMPS [21], AFORS-HET [22], and SCAPS-1D [23][24] commonly used in the thin-film PV community; as well as more sophisticated programs for 2D and 3D modeling.

For the models that may be more easily reduced to analytical expressions, simple MATLAB and Mathematica calculations may suffice to do sensitivity analyses or parameter fittings. In the present work, both numerical and analytical tools are employed to simulate and predict cell performance. This chapter will detail the equations used in modeling, as well as the tools used to perform such modeling, and input parameters used.

2.1 Electron Transport Differential Equations

Modeling carriers in semiconductors requires equations for the (i) transport of carriers under electrochemical potential gradients, and (ii) generation of carriers by thermal or optical means, (iii) recombination of free carriers by a variety of processes. These will be independently treated, then combined in the following section.

2.1.1 Diffusion and Drift

Free holes and electrons move under concentration gradients (diffusion) and electric potential gradients (drift). In doing so, the hole and electron distributions influence the concentration and potential gradients, resulting in a set of coupled differential equations.

The first of these is Poisson's equation, providing the relationship between charge density and electric field strength $\vec{E}$. The net charge density may come from the fixed acceptor density N_{A}, fixed donor density N_{D}, as well as free hole density p, and free electron density n, all with units of cm^{-3}:

$$\frac{dE}{dx} = \frac{q}{\varepsilon}(p(x) - n(x) - N_{\mathrm{A}}(x) + N_{\mathrm{D}}(x)), \tag{2.1}$$

where $q = 1.602 \times 10^{-19}$ C is the charge of an electron, and $\varepsilon = \varepsilon_r \varepsilon_0$, where ε_r is the relative dielectric permittivity as compared to the absolute permittivity of vacuum, $\varepsilon_0 = 8.854 \times 10^{-12}$ F/m.

Next, the transport equations describe the hole and electron currents that result from both drift and diffusion contributions:

$$J_n = q\mu_n nE + qD_n \frac{dn}{dx} \tag{2.2}$$

$$J_p = q\mu_p pE - qD_p \frac{dp}{dx}. \tag{2.3}$$

Here, J represents the current density in $\mathrm{mA/cm^2}$ and μ is the mobility in $\mathrm{cm^2/V{\cdot}s}$, for electrons and holes respectively. The pre-factor to the electric field may be recognized

as the conductivity, a product of mobility, carrier density, and the fundamental charge. D is the carrier diffusivity in cm^2/s. Diffusivity and mobility of carriers are related by Einstein's relationships through the thermal energy, where $k_B = 8.617 \times 10^{-5}$ eV/K is the Boltzmann constant. This is true for band conductors, which is presumed to be accurate for Cu_2O, and may break down for dispersive hopping transport in defective or nano-crystalline materials.

$$D_n = \frac{k_B T}{q} \mu_n \tag{2.4}$$

$$D_p = \frac{k_B T}{q} \mu_p. \tag{2.5}$$

Thus far, the system of equations is independent of time. Continuity equations introduce the time variable, by combining the motion of carriers with their recombination (sink) U, and generation (source) G terms (units of $cm^{-3}s^{-1}$):

$$\frac{dn}{dt} = \frac{1}{q}\frac{dJ_n}{dx} - (U - G) \tag{2.6}$$

$$\frac{dp}{dt} = -\frac{1}{q}\frac{dJ_p}{dx} - (U - G). \tag{2.7}$$

In steady state, the time derivatives are zero, allowing for a 1-D solution in x to the system of equations. First, however, the nature of the recombination and generation terms must be defined.

2.1.2 Generation of Carriers

The propagation and absorption of light is governed by the index of refraction n, and extinction coefficient k, which determine the absorption coefficient: $\alpha = 4\pi k/\lambda_0$. To accurately model generation, a full solution of the Maxwell equations with n and k over the volume of the device could determine a 2-D or 3-D generation profile. A more simple approximation arises in the case of 1-D absorption. Here, we assume the generation rate is proportional to the rate of change of intensity of light propagating through a film, multiplied by the number of photons incident at the absorber surface,

$N_{\text{ph,i}}$. This simple form ignores the possibility of 2-D or 3-D inhomogeneities, back reflection, or other internal reflections.

$$G(\lambda, x) = \alpha(\lambda) N_{\text{ph,i}}(\lambda) e^{-\alpha(\lambda)x} \tag{2.8}$$

Not all externally incident photons, $N_{\text{ph,e}}$, make it into the absorber; there are front transmission T_{front}, and reflection R_{front} losses: .

$$N_{\text{ph,e}}(\lambda) = N_{\text{ph,i}}(\lambda)[1 - R_{\text{front}}(\lambda)][1 - T_{\text{front}}(\lambda)] \tag{2.9}$$

Integrating the generation profile over all wavelengths, with the AM1.5 spectrum of photon flux per wavelength range, would yield the total maximum photocurrent. However, in a real solar cell, not all generated photocarriers are collected due to recombination, to be discussed in the ensuing chapter.

The absorption coefficient of Cu_2O is unique, as despite having a direct bandgap, its crystallographic inversion symmetry prohibits the direct band-to-band optical excitation at the Γ point [25]. Thus, the absorption strength is lower initially at the bandgap of approximately 2.0 eV (620 nm), but then increases around 2.5 eV (500 nm) as seen in Fig. 2-1. Absorption is improved near the bandgap by excitonic effects, thus the calculation of absorption coefficient varies between sources depending on the consideration of excitonic absorption. Malerba *et al.* [25] and Sopra's [26] ellipsometric measurements differ in their absorption coefficient in the longer wavelengths. In addition, given the difficulty of experimentally calculating the absorption coefficient on thin-film Cu_2O samples with high degrees of surface texture (and back reflectance), it is difficult to extract accurate absorption coefficient data over the entire wavelength range. The geometric mean of Sopra and Malerba's expected absorption coefficients seems to best match the UV-VIS spectrophotometric measured absorption coefficient on sputtered films at long wavelengths > 500 nm. This average absorption coefficient appears to accurately model the spectral response of thin-film cells in the long wavelengths, however Malerba's absorption coefficient models both thick foil and thin-devices best. Thus, Malerba's α data is used for the present simu-

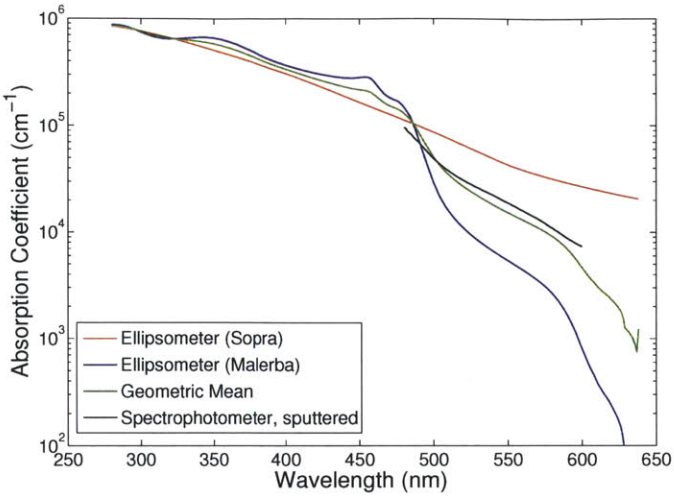

Figure 2-1: Cu_2O absorption coefficient calculated from n and k data collected by Malerba [25] and Sopra [26], as well as that measured by spectrophotometry on sputtered films. The geometric mean of the two ellipsometry data series matches well to experimental data on sputtered films. Malerba's absorption coefficient is used in the present work.

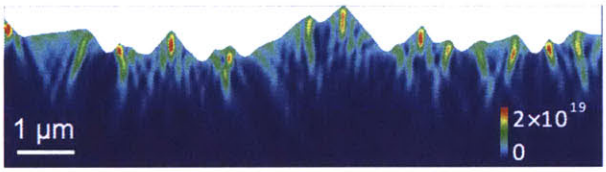

Figure 2-2: Cu_2O free carrier generation for 500 nm incident light, in units of $cm^{-3}s^{-1}nm^{-1}$ [27]. The non-uniformity of generation is clear, but can be approximated with a 1-D absorption generation profile.

lations, over the 300-630nm wavelength range. Inaccuracies in the spectral response models using Malerba's absorption coefficient can be attributed to the 3D textured nature of the film.

The generation profile can be made more accurate by computing Maxwell's equations over a 2-D or 3-D film stack with complex geometry, and may be performed by Finite Difference Time Domain (FDTD) methods. This calculation was performed by Jonathan Mailoa and published with Lee *et al.* [27]. The generation profile over a 2.5 μm textured film in FDTD is plotted in Figure 2-2. This generation profile exhibits non-uniform absorption as a function of depth. Future simulations should take into account this inhomogeneity, but for simplicity they will not be used in the present work.

2.1.3 Recombination

In steady state, all generated carriers will recombine or leave the device as output current. An increased generation rate thus corresponds to increased output current and/or increased recombination. Understanding the driving forces for recombination is therefore critical for modeling. All recombination models depend upon the concentrations of electrons and holes:

$$n = n_0 + \Delta n \tag{2.10}$$

$$p = p_0 + \Delta p, \tag{2.11}$$

where $\Delta p = \Delta n$ are the injected hole and electron densities. The dark electron and hole concentrations are related by the intrinsic carrier concentration, $n_i^2 = n_0 p_0$.

In radiative recombination, a conduction band electron and valence band hole recombine to emit a photon of the bandgap energy. The probability of this recombination is dependent upon the carrier concentrations by a proportionality constant; the rate of recombination $U_{\text{rad}} = Bnp$. In the dark, this is proportional to the intrinsic carrier concentration squared. Under high illumination conditions, on the other hand, where Δn is much greater than n_0 and p_0, this is proportional to the injected carrier concentration squared. This form of recombination may be mitigated by photon recycling, by reducing the possible solid angle of emission, or by reducing the emitted photon density of states.

In Auger recombination, an electron and hole recombine and give their energy to a conduction band electron. This form of recombination only occurs for higher majority carrier concentrations. In a p-type material, this may be approximated as $U_{\text{ehh,Auger}} = C_p n p^2$ [28].

Finally, the most critical form of bulk recombination for Cu_2O is Shockley-Read-Hall (SRH) recombination through defect levels. Here, an electron or hole is captured in a midgap defect level, or "trap". Depending on the binding energy of this trap (E_T), it will remain there until it is re-emitted, or recombines with a carrier of the opposite type. This recombination dominates in defective materials, especially if the

defect energy levels are mid-gap. The SRH model describes this mechanism fully by considering the local temperature- and electrochemical potential dependence of defect occupation.

$$U_{\mathrm{SRH}} = \frac{(np - n_i^2)}{\tau_{p0}(n + n_1) + \tau_{n0}(p + p_1)}, \tag{2.12}$$

where:

$$\tau_{n0} = \frac{1}{N\sigma_n v_{\mathrm{th}}} \tag{2.13}$$

$$\tau_{p0} = \frac{1}{N\sigma_p v_{\mathrm{th}}}, \tag{2.14}$$

and:

$$n_1 = N_{\mathrm{C}} \exp\left(\frac{E_{\mathrm{T}} - E_{\mathrm{C}}}{k_B T}\right) \tag{2.15}$$

$$p_1 = N_{\mathrm{V}} \exp\left(\frac{E_{\mathrm{C}} - E_{\mathrm{g}} - E_{\mathrm{T}}}{k_B T}\right). \tag{2.16}$$

Here, N_{C} and N_{V} are the conduction band and valence band densities of states, respectively, v_{th} is the carrier thermal velocity, and σ is the carrier capture cross-section. E_{T} and E_{C} are defined relative to the valence band. The solution to this equation is complex, but can be simplified by recognizing that in a p-type material, there are many orders of magnitude more holes than electrons. Thus, $n \ll p$, and the minority carrier electron lifetime τ_{n0} becomes much more critical, and the SRH recombination rate depends on excess electron density as:

$$U_{\mathrm{SRH}} \approx \frac{\Delta n}{\tau_n} \tag{2.17}$$

A specific form of this defect-assisted recombination occurs at interfaces, and is captured by the surface recombination velocity S_{i}, as a function of interface state density N_{i}^*:

$$S_{\mathrm{i}} = v_{\mathrm{th}} \sigma N_{\mathrm{i}}^*. \tag{2.18}$$

This allows for each interface in a device solver to be treated as a single node with

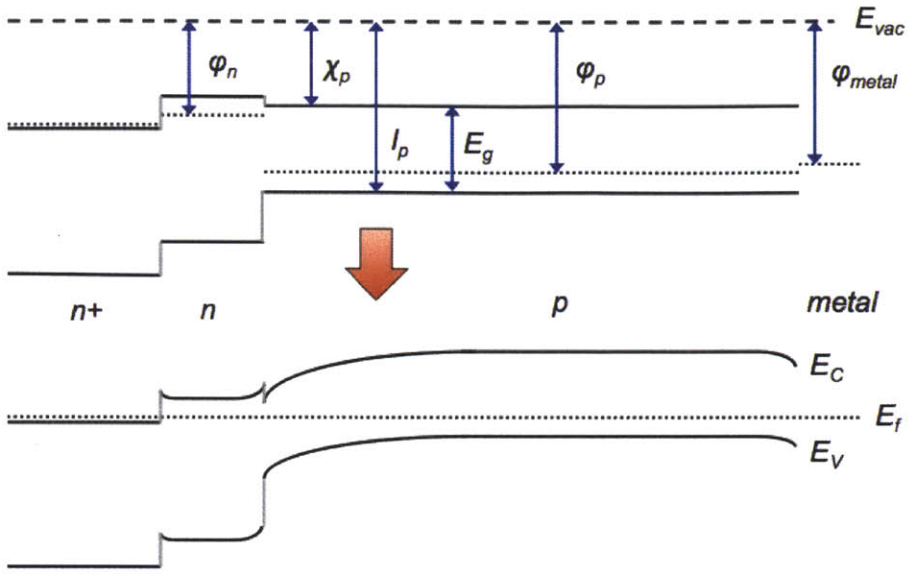

Figure 2-3: A typical heterojunction band diagram assuming continuous electric displacement $\vec{D}$ and potential across the junction, *top*, before electrochemical equilibrium, *bottom*, after electrochemical equilibrium has been achieved. The horizontal axis is position through the device, while the vertical axis is energy relative to vacuum. Each layer is defined by its electron affinity χ, bandgap E_g, ionization potential I, and electrochemical potential or work function ϕ. The junction built-in voltage is set by the difference in electrochemical potentials across the junction.

its own recombination activity, similar to the bulk.

2.1.4 Junction Formation

A typical heterojunction is pictured in Fig. 2-3, assuming a continuous electric displacement $\vec{D}$ and potential across the junction, both before and after equilibration.

The process of charge transfer across the junction can be described by the Poisson equation above, in steady state where the time-derivative terms are zero, and the drift and diffusion currents balance. A numerical package can solve this system of equations by considering finite 1-D domains in x throughout the junction, and simultaneously computing the electric field, potential, and current output current of the device at a variety of input conditions – especially different generation rates. Solar cell performance parameters are then extracted from this output $J - V$ curve, and can accurately model the physics of a real solar cell. More complicated phenomena such as the capacitance, or the quantum efficiency, may also be readily simulated

numerically.

It is occasionally desirable to simplify these numerical equations to analytical expressions for the built-in potential or barrier height of a junction, as well as the output current and other device properties. In Appendix A, a variety of analytical expressions are derived based on different simplifying boundary conditions and assumptions. These models may then be used in analytical solvers to obtain quicker, but simpler, results.

2.2 Simulation in SCAPS-1D

2.2.1 Program Overview

SCAPS-1D is a program developed by Marc Burgelmann, as a 1-D numerical optoelectronic device solver specifically targeted at thin-film stacks [23] [24]. It particularly excels at simulating capacitive properties, and is much more commonly used to simulate thin-film heterojunctions than PC1D (used for crystalline silicon). The program solves the Poisson, drift-diffusion, and continuity equations simultaneously to determine dark or illuminated $J-V$, $C-V$, $C-f$, and external quantum efficiency (EQE) curves. The program handles heterojunctions by adding additional nodes at the interfaces, which can determine surface recombination or surface charge, all tied to defect occupation probability.

To define a simulation in the program, one inputs the layer stack and respective thicknesses first (Fig. 2-4). These layers may be conductive front and back contacts, or semiconductors of p, i, or n doping.

Each layer may then be defined using the bulk material's bandgap E_g, electron affinity χ, mobility, conduction band and valence band density of states, absorption coefficient, thermal velocity, and defect densities and energy distributions (which will determine lifetime), as in Fig. 2-5. These properties may all be graded within each layer. Similarly, each interface may have a specific defect distribution which determines the surface recombination velocity at that interface.

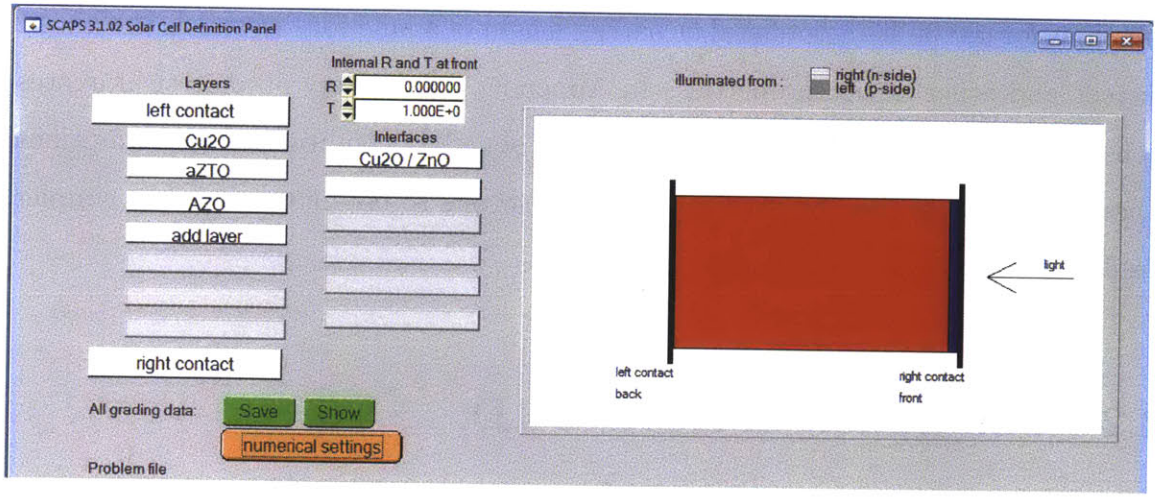

Figure 2-4: The input window for inputting cell geometry and layer stacks in SCAPS. From here, bulk layer properties as well as interface defects may be defined. The front and back contacts may have optical transparency/reflection, as well as a work function and thermal velocity.

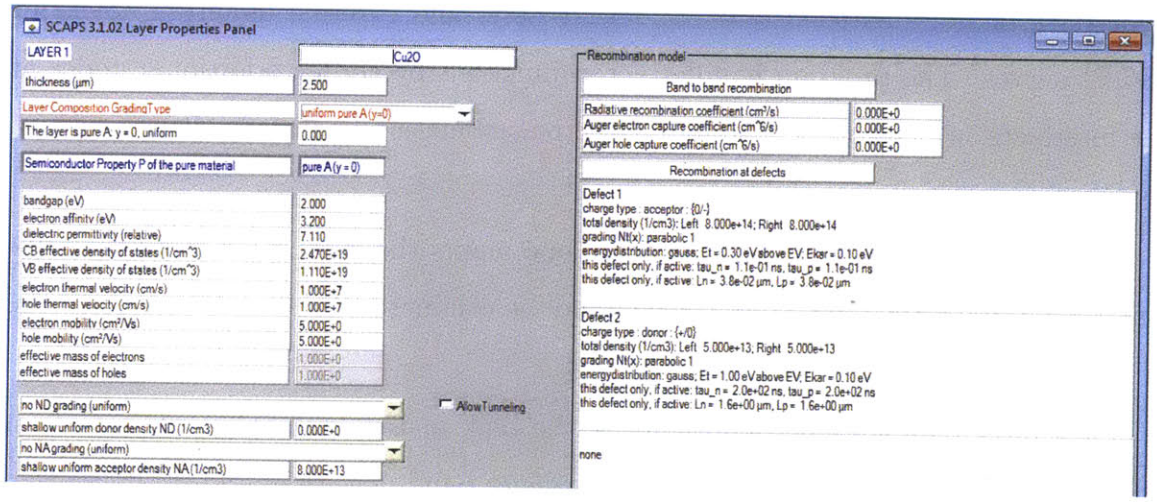

Figure 2-5: An input window for defining specific bulk properties of a layer in SCAPS, including transport, electronic, optical, and defect properties.

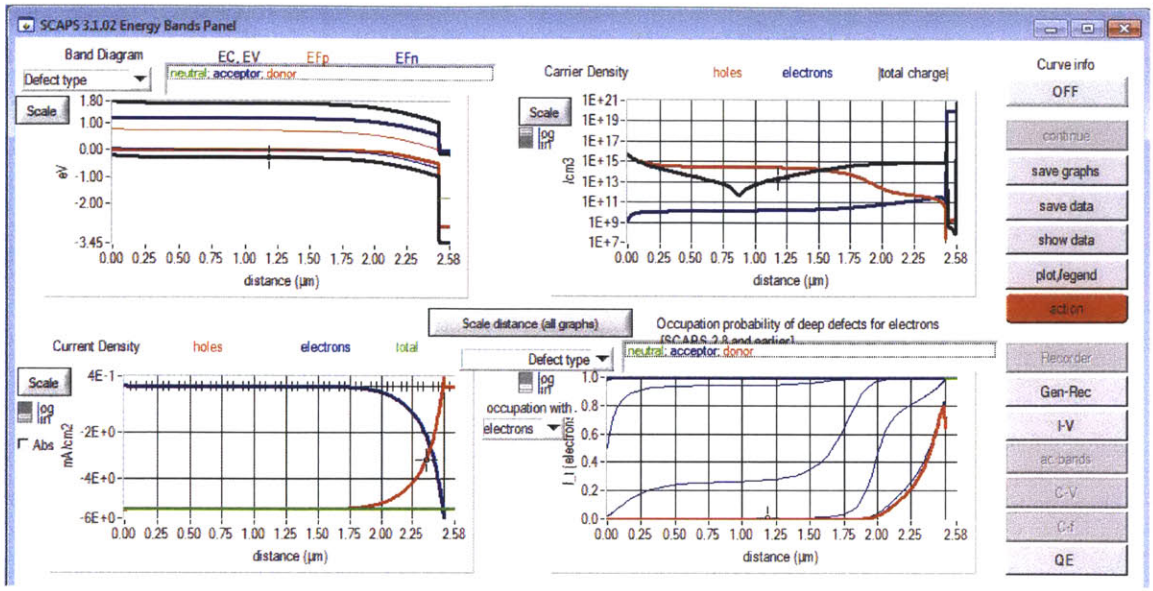

Figure 2-6: The band alignment and carrier statistics, current density, and defect occupation provided by SCAPS in a standard simulation. Other output windows include quantum efficiency, $J-V$, and capacitance as a function of voltage and frequency.

Once a simulation has been set-up, operating conditions such as illumination profile and temperature are defined. A simulation output appears as in Fig. 2-6.

2.2.2 Cu_2O and Device Properties

The properties used for modeling Cu_2O films are a combination of experimental as well as literature data. They are listed in Table 2.1, with references where pulled from literature. Mobility and acceptor densities are adapted from recent measurements on electrochemically deposited Cu_2O [29]. Compensation ratios of 2-5 (acceptors:donors) are estimated from the review performed by Biccari [30], which matches sputtered film data [7].

Thermally oxidized Cu_2O foils tend to exhibit lower carrier concentrations down to 1×10^{13} cm^{-3}, and higher mobilities up to 100 $cm^2/V\cdot s$ [30]. Meanwhile, sputtered films in our lab have exhibited mobilities between 1-60 $cm^2/V\cdot s$, and carrier concentrations in excess of 1×10^{16} cm^{-3} [7].

The most uncertain of these properties is that of the defect energy levels, which have been examined through both computational density functional theory (DFT)

Table 2.1: Cu_2O bulk properties

Property	Value	Reference
E_g	2.0 eV	[7]
χ	3.2 eV	[31]
N_C	2.47×10^{19} cm^{-3}	[30]
N_V	1.11×10^{19} cm^{-3}	[30]
ε_r	7.11	[30]
μ_n	1 cm^2/V·s	[29]
μ_p	1 cm^2/V·s	[29]
N_A	1×10^{14} cm^{-3}	[29]
$E_{T,A}$	0.3 eV	[30] [32]
N_D	5×10^{13} cm^{-3}	[30]
$E_{T,D}$	1.0 eV	[30] [32]

as well as experiment. Temperature-dependent Hall-effect measurements suggest an acceptor activation energy of 0.23 eV, with compensation by a donor [7]. Deep-level transient spectroscopy by Paul *et al.* identified two acceptor traps at 0.2 eV and 0.5 eV above the valence band [17]. DFT calculations identify the copper vacancy is the source of the primary acceptor trap, around 0.2-0.4 eV, with a higher binding energy split copper vacancy as well [30][32]. The nature of the compensating donor is not known; the oxygen vacancy would be the most likely, but is not charged in the gap. Split copper vacancies and oxygen interstitials sit midgap around 1 eV, but should exhibit acceptor character [32]. It is this author's opinion that an amphoteric defect such as H, or an extrinsic impurity in the source material, could be producing this compensating donor.

Thin-film solar cells typically employ a stack that includes an absorber, a "buffer" layer of opposite doping type, a transparent conductor ("window" layer), as well as front and back metal contacts. The front window layer and metallization must result in minimal shading and reflection losses, while simultaneously retaining high conductivity. This makes the selection of the n-type layer paired with Cu_2O very important. In the vast majority of cells produced here, this n-type material is ZnO. Its properties are catalogued in Table 2.2.

As a preliminary test, the band bending and alignment for a variety of Cu_2O/ZnO

Table 2.2: ZnO bulk properties

Property	Value	Reference
E_g	3.3 eV	[24]
χ	4.3 eV	[24]
N_C	2.2×10^{18} cm^{-3}	[24]
N_V	1.8×10^{19} cm^{-3}	[24]
ε_r	9.0	[24]
μ_n	10 cm^2/V/s	
μ_p	10 cm^2/V/s	
N_A	N/A	
$E_{T,A}$	N/A	
N_D	$10^{18} - 10^{20}$ cm^{-3}	
$E_{T,D}$	0.01 eV	

junctions can be simulated in SCAPS, as seen in Fig. 2-7. As the hole concentration drops below 1×10^{14} cm^{-3}, the Cu_2O becomes fully depleted through the entire 2 μm absorber. Analytical expressions can be used to describe the junction potential.

2.3 MATLAB Analytical Models

2.3.1 Junction Formation

In Appendix A, analytical equations for depletion depth W, and built-in voltage V_{bi}, are defined for a p-n heterojunction. The most important quantities to determine are the built-in potential in the p-layer specifically, referred to as V_{jp}, and W. For a simple p-n^+, heterojunction, in which the entire depletion region occurs in the Cu_2O layer, the p-layer built-in potential is:

$$V_{jp} = (V_{bi} - V_A)\left(\frac{\varepsilon_{r,n} N_D}{\varepsilon_{r,n} N_D + \varepsilon_{r,p} N_A}\right). \tag{2.19}$$

In addition, the depletion depth in the p-type layer is:

$$W_p = \left(\frac{2\varepsilon_{r,p}\varepsilon_0 V_{jp}}{qN_A}\right)^{1/2}. \tag{2.20}$$

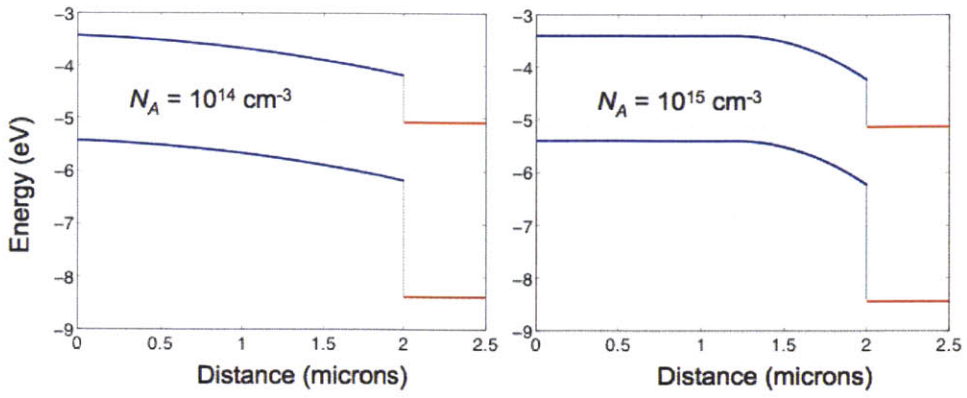

Figure 2-7: Preliminary un-illuminated band alignment and band bending in Cu_2O (blue) / ZnO (red) junctions at different carrier concentrations, calculated in MATLAB. Low carrier concentrations in Cu_2O result in full depletion through the depth, and a linear electric field.

Given these two properties, the electric potential in the depletion region is quadratic:

$$V(x) = \frac{qN_A}{2\varepsilon_{r,p}\varepsilon_0}(x + W_p)^2, \quad \text{for} - W_p < x < 0. \tag{2.21}$$

Using these equations, the devices' band structures may be calculated analytically, and used to predict a number of device properties including collection efficiency and capacitance, among others.

2.3.2 Collection and Quantum Efficiency

In the same way that the generation profile for free electrons is a function of depth through the material (and photon wavelength), the collection probability for those same electrons is also a function of depth in the device. A full numerical device simulator would use the concentration profiles of electrons and holes and their recombination statistics to predict how many photo-generated carriers make it to the junction and get collected. If these carriers move purely by diffusion towards the junction, their collection will decay exponentially as they are generated further from the junction. The characteristic length of this exponential is the diffusion length:

$$L_{\text{diff}} = \sqrt{D\tau} = \sqrt{\frac{k_B T}{q}\mu\tau}, \tag{2.22}$$

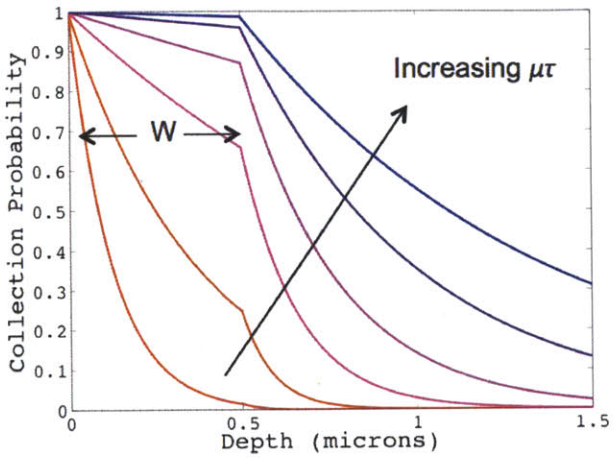

Figure 2-8: The changing strength of diffusion and drift collection as a function of carrier mobility-lifetime product. At high mobility-lifetime products, the profile reduces to that used in c-Si, with 100% collection in the depletion region followed by exponential decay outside of it. At low $\mu\tau$ products, the collection is purely within the depletion region. These profiles assume a surface recombination velocity of zero at the front and back surfaces.

where τ is the bulk lifetime. In crystalline silicon photovoltaics, where the length of the depletion region is much smaller than the thickness of the Si wafer, it is often assumed that 100% of carriers generated in the depletion region are collected. Then, the collection probability decays exponentially into the bulk. However, in thin absorber materials where the depletion region makes up a majority of the device, and where the carrier lifetimes are small enough, the 100% collection approximation breaks down. In this case, it is necessary to define a "drift length" counterpart to the diffusion length. This collection length applies to carriers in the depletion region instead, where $x < W$:

$$L_{\text{dr}} = E_{\text{avg}}\mu\tau = \frac{V_{\text{bi}}}{W}\mu\tau. \tag{2.23}$$

The combination of these two collection profiles results in a piecewise function:

$$P_{\text{C}} = \begin{cases} \exp(-x/L_{\text{dr}}) & \text{if } x \leq W \\ \exp(-W/L_{\text{dr}})\exp(-(x-W)/L_{\text{diff}}) & \text{if } x > W \end{cases} \tag{2.24}$$

These profiles are plotted in Fig. 2-8 for a range of $\mu\tau$ products. Multiplying the generation and recombination profiles, and integrating over all wavelengths, gives the total photocurrent.

2.4 Fitting Routines

Once the $I-V$ and QE characteristics of a cell are measured, they can be compared to simulation to fit each parameter. The immense number of fitting parameters, and the relatively small amount of collected data are together sub-optimal for fitting with classical or even Bayesian statistics—this can result in high precision, but low accuracy. However, when using the analytical expressions for collection and $I-V$ curves, there are fewer fitting parameters, and simple classical statistics can be used to fit parameters.

In both cases, parameters were adjusted manually and found to minimize error by the least-squares method. This fitting allowed for the prediction of transport and junction properties, but runs the risk of identifying a single solution which is not unique. It cannot easily evaluate the uncertainty of a given set of parameter fits, and furthermore it is not clear that this certainty in parameter fitting is useful, given the model uncertainty in our analytical expressions, the uncertainty in experimental data, and the uncertainty in the fixed parameters such as absorption coefficient.

An interesting project in this realm would be the construction of a Bayesian statistical tool that, given a set of analytical expressions for device performance, several unknown variables, and device output data, could infer the value and uncertainty of each variable. The accuracy of this fit would then be dependent upon the amount of data taken. Temperature- and bias-dependent collection, current, and capacitance measurements, as well as auxiliary reflectance and absorptance measurements, would together ensure an accurate variable inference. However, this multi-parameter and multi-output fit cannot be done manually, and must be done computationally.

Chapter 3

Fabrication of Cu_2O Cells

The formation of high-quality Cu_2O cells necessitates high quality component films, smart cell design, and careful fabrication procedures. In producing Cu_2O devices, a variety of cleaning and deposition methods were utilized. These methods are described in the present chapter.

3.1 Deposition of Cu_2O

Cu_2O may be deposited through a variety of techniques. The original and most common process involves thermally oxidizing a thin copper foil at high temperatures [4]. The high diffusivity of copper at high temperatures allows for oxidation of 100 micron foils in 1-2 hours [11]. However, at ambient oxygen partial pressures, the CuO phase is more stable than Cu_2O, as seen in the Cu-O phase diagram, Fig. 3-1. Thus, oxidation must be performed at $T = 1050$ K and low oxygen partial pressures, and during cooling a thin surface layer of CuO forms at lower temperatures, which must be removed.

The advantage of this process is in its ability to achieve large-grain, low defect-density Cu_2O with high temperatures and long annealing periods. However, the process is time and energy intensive, and produces unnecessarily thick films. It is desirable to use a less capital-intensive, rapid, thin-film deposition technique to form the Cu_2O layer. For this, sputtering and electrodeposition are possible.

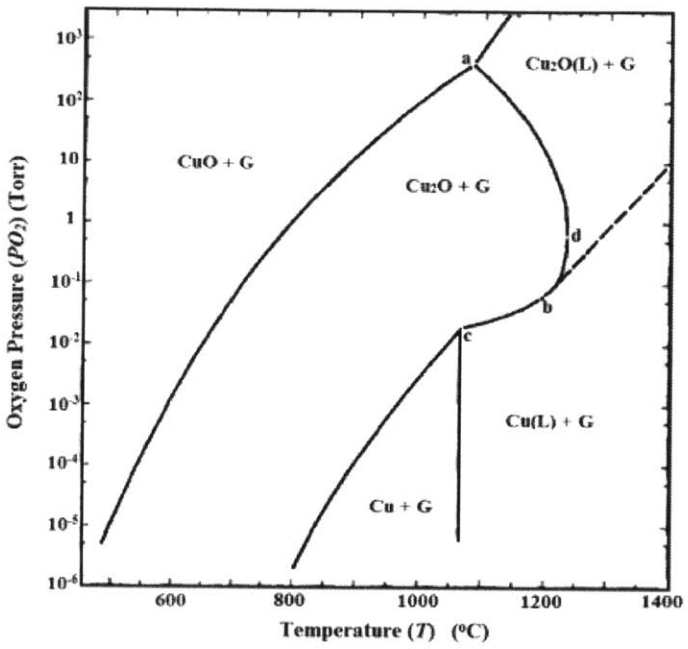

Figure 3-1: Cu_2O phase diagram demonstrating most stable equilibrium phases by temperature and oxygen partial pressure [33].

3.1.1 Sputtering

Cu_2O ceramic targets are frequently used for thin-film sputtering, with the option of flowing oxygen gas to tune the film stoichiometry. Furthermore, reactive DC magnetron sputtering allows for a higher degree of tunability, by using a pure Cu target. In this way, the flux of copper ions and oxygen ions may be independently controlled.

The optimization of reactive Cu_2O deposition was performed by Lee *et al.* [7] prior to the present work, and it was found that especially at high temperatures, high mobilities of $\mu = 60$ cm^2/V·s were achieved, approximating that of thermally oxidized foils.

However, in real device stacks, delamination and chemical interdiffusion will occur at higher deposition temperatures. Thus, for sputtered Cu_2O devices, the temperature was held at 200°C. Chamber pressures ranged from 1.3-10 mTorr. These films were sputtered in both substrate and superstrate configurations, which will be discussed in the following section.

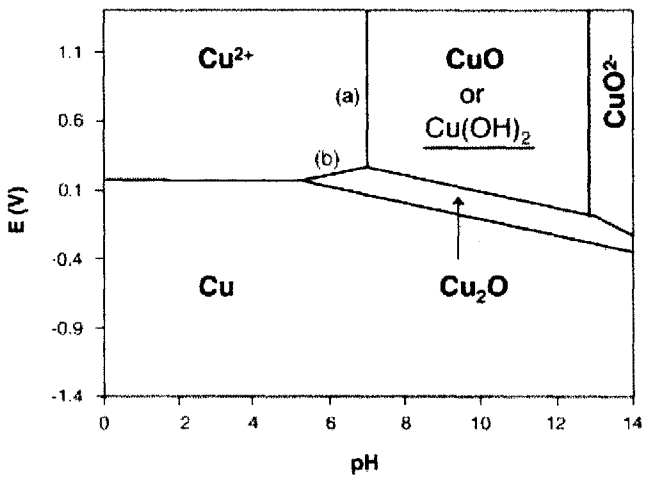

Figure 3-2: Pourbaix diagram for Cu in aqueous solutions, showing the most stable phases as a function of potential and pH [34].

3.1.2 Electrochemical Deposition

The Pourbaix diagram of Cu (Fig. 3-2) in an aqueous environment suggests that there is a window of phase stability for Cu_2O in an alkaline solution. This may be exploited to achieve phase-pure electrochemical deposition of Cu_2O on a conductive substrate.

The recipe for this deposition has been adapted from that of Mizuno *et al.* [29]. The deposition solution uses hydrated copper sulfate powder ($CuSO_4 \bullet 5H_2O$) as the copper ion source, at 0.4 mol/L concentration. This solution is buffered to a higher pH with a 1 mol/L sodium hydroxide NaOH solution. In a more alkaline pH, the Cu^+ ion becomes more stable than the Cu^{2+} ion, allowing for deposition of cuprous oxide rather than cupric oxide. In addition, 3 mol/L lactic acid is added to the copper sulfate solution to act as a complexing agent. For all of the cells fabricated in the present work, a pH of 12.5 used. Unless otherwise noted, a current density of -0.27 mA/cm^2 was used. This current density results in pure phase Cu_2O at high deposition rates of approximately 1.25 microns per hour.

The deposition bath includes two electrodes in solution – the counter electrode is a positively biased Pt film, while the substrate is the negatively biased working electrode and is typically a gold film for high conductivity and stability in alkaline

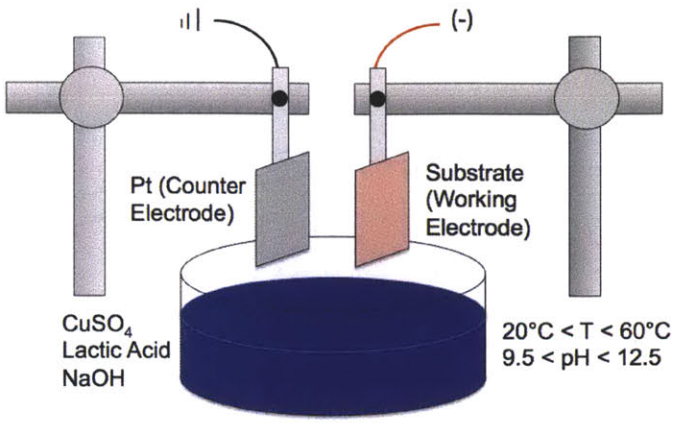

Figure 3-3: Configuration for two-electrode deposition bath, including electrodes and sourcemeter. The deposition solution is a deep blue colour as a result of the Cu^+ ions (as opposed to the light blue colour of the aqueous Cu^{2+} ion).

pH. The electrodes are placed one inch apart, as shown in Fig. 3-3.

Optimization of the deposition recipe began with a series of current density scans, at constant pH. It was found that higher current densities led to a larger potential difference between the counter and working electrodes, which resulted in preferential deposition of Cu instead of Cu_2O. In addition, a pH of 12.5 was selected, which yielded lower resistivity Cu_2O and the highest performing devices. A deposition temperature of 40°C was chosen, as the higher temperature yielded higher quality films and more uniform growth. At higher temperatures than this, the rate of water evaporation can lead to incomplete film coverage and time-dependent solution concentration.

As the films can only be deposited on a conductive substrate, it is difficult to independently extract the conductivity or Hall effect mobility of the films. Mizuno was able to measure the transport properties using a lift-off procedure. For the same deposition conditions, at pH = 12.5, and for 2 micron films, hole concentrations were 10^{14} cm^{-3}, and Hall effect mobility was measured as approximately 1-2 $cm^2/V{\cdot}s$. This mobility closely correlated with grain size, while the carrier concentration increased with decreasing stoichiometric Cu content in the films, consistent with the formation of Cu vacancies [29].

3.2 Device Structure

In general, the device structure closely resembles a typical thin-film heterojunction. The device consists of a thin-film p-type Cu_2O absorber layer, in a heterojunction with an n-type material. This n-type material may be paired with, or may itself be, a transparent conducting oxide (TCO). The semi-transparent front contact may include metal finger electrodes to lower series resistance. On the back side relative to illumination is a conductive metal contact, which does not have to be transparent. The order in which these layers are successively deposited can vary, either in the substrate or superstrate configuration.

3.2.1 Superstrate

In the superstrate configuration, the front contact is deposited on a glass substrate first. This is typically a highly conductive TCO layer. For this purpose, indium tin oxide (ITO), fluorine-doped tin oxide (FTO), or aluminum doped zinc oxide (AZO) were used, typically purchased pre-coated. Sheet resistance for each film was $<$ 10 $\Omega/\square$, on a 1-2 μm film. The advantage of beginning with TCO deposition is that it allows for high temperature and higher energy sputtering methods, which may yield higher quality TCOs, but would otherwise damage the previously deposited layers.

The layer stack is shown in Fig. 3-4, similar to a typical CdTe deposition sequence. After the TCO and ZnO buffer layer deposition, the absorber may be sputtered or electrodeposited, followed by the evaporation of the back contact. This structure is favoured in CdTe manufacturing because it allows for more precise control over the back contact properties.

3.2.2 Substrate

Substrate devices involve the same layers and geometry, but are deposited in the reverse order starting with the back contact. As some metals do not adhere directly to glass, a seed or adhesion layer must first be deposited. Here, a thin 5 nm titanium layer is used. Next, the metal back contact is evaporated, followed by absorber

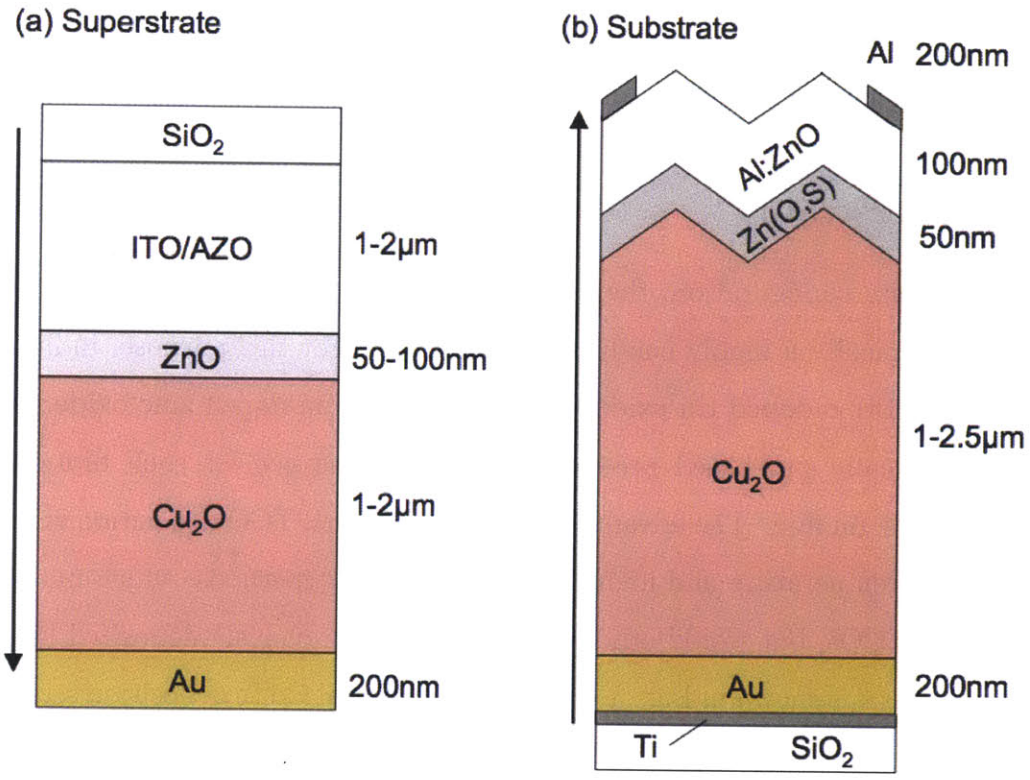

Figure 3-4: Typical layout of (a) a superstrate-style cell on glass, and (b) a substrate-style cell on glass or oxidized Si wafer.

deposition.

In this configuration, the n-type material and TCO may be deposited by sputtering. However, to achieve more conformal coverage, and a lower power deposition, atomic layer deposition (ALD) is preferred. ALD is a form of pulsed chemical vapour deposition where gaseous precursors for each element are delivered successively to build up a thin-film coating nearly atom-by-atom. ALD offers a number of advantages, and is most practical and useful in the substrate configuration.

The substrate configuration allows for slightly more control over the substrate properties, as well as the reflectivity of the front surface. In general, depositions should run in order of highest to lowest temperature, making the substrate technique favourable for low-temperature front layer depositions and/or high temperature absorber depositions.

3.3 Cleaning Procedures

Perhaps the most underemphasized and yet most critical feature of device fabrication is the cleaning routine, as well as all efforts to maintain purity of bulk and surface properties during fabrication and transportation. Extrinsic impurities in concentrations of parts per million can strongly influence bulk transport properties, monatomic adsorbed surface layers can significantly affect interface properties, and organic contaminants such as dust and oils can create pinholes and shunts, and in turn ruin device performance.

Initially, the standard device cleaning procedure included five minute ultrasonication steps in acetone and isopropanol (IPA) in sequence, followed by compressed nitrogen drying. The samples were then stored in standard plastic sample cases with 1 x 1 in^2 holders, where the sample cases were previously blown with compressed N_2. These samples were then frequently transported outside between the PV Lab and joint-use facilities including Harvard Center for Nanoscale Systems (CNS) and MIT Electronic Materials Lab (EML).

In the initial batches of devices (primarily superstrate sputtered Cu_2O), many

devices were highly shunted, even ohmic. Some commercial substrates such as the FTO-coated glass were found to have a thick oil coating and other organic contamination. In response, new procedures to ensure cleanliness were implemented, as follows:

1. Before dicing the Si or quartz substrates, spin-coat with PMMA photoresist (2000 RPM, 40 seconds, no bake) to protect surface
2. Post-dicing, ultrasonicate in DI water for 5 minutes (all performed in cleanroom)
3. Ultrasonicate in acetone for 5 minutes (do not let it dry between steps)
4. Ultrasonicate in IPA for 5 minutes
5. Ultrasonicate in DI water for 5 minutes
6. Blow dry with N_2 gas
7. For glass or Si/SiO_2 substrates, treat the substrates in O_2 plasma (Harvard CNS Anatech, 100 W, 5 minutes)

Transportation and storage are equally important, given the sensitivity of devices to contamination, especially at interfaces. Time between subsequent depositions was minimized so that no more than one day would elapse between each step. Sample cases were switched to petri dishes, which have been sterilized and thus have no particulate or organic matter before opening. These cases are then sealed with an adhesive plastic wrap to provide a temporary moisture barrier. When not in use, the samples are stored in an N_2 glovebox environment.

3.4 Full Process Flow

The following list details each of the process steps involved in cell fabrication for superstrate- and substrate-style cells (Figs. 3.1 and 3.2 respectively), as well as for cell photolithographic isolation (Fig. 3.3). Specific masks are labelled and shown in the figures below.

Table 3.1: Superstrate deposition sequence and parameters

Layer	**Tool**	**Location**	**Recipe**
Glass/ TCO	Dicing saw	MIT ICL	G-Mode, speed 5, 2-3 cuts, 25.4 mm offset
ZnO	Sputterer (AJA)	ONE Lab or MIT EML	ZnO target, 150 W, 20 mTorr, 12 sccm Ar, "200°C", 60 minutes (150 nm), mask Fig. 3-5(a)
Cu_2O	Sputterer (PVD)	PV Lab	Cu target, 30 W, 4 mTorr, 40 sccm Ar, 4 sccm O_2, "200°C" 120 minutes (1 μm), mask Fig. 3-5(b)
Au	E-beam Evaporator (EE-4)	Harvard CNS	200 nm (0.2 nm/sec), mask Fig. 3-5(c)

Table 3.2: Substrate deposition sequence and parameters

Layer	**Tool**	**Location**	**Recipe**
Si/SiO_2	Dicing saw	MIT ICL	A-Mode with 25.79 mm y-offset, 0.25 mm z-offset
Au	E-beam Evaporator (EE-4)	Harvard CNS	5 nm Ti adhesion layer (0.1 nm/sec), 200 nm Au (0.2 nm/sec), mask Fig. 3-6(a)
Cu_2O	Electro-deposition	PV Lab	70 mL $CuSO_4$/lactic acid solution, buffered with NaOH (≈130mL) to pH = 12.5, T = 40°C, J = -0.27 mA/cm^2, 1" separation from Pt counter electrode, unilluminated, 120 minutes (2.5 μm)
Zn(O,S), Al:ZnO	ALD	Harvard Gordon Lab	50 nm Zn(O,S) (diethyl zinc, H_2O, H_2S) and 100 nm Al:ZnO (1:20 trimethyl aluminum with diethyl zinc, H_2O) at 120°C, with 60 minute pre-deposition bake at temperature
Al	E-beam Evaporator (EE-3)	Harvard CNS	-12 kV, 0.06 A with 40 min. ramp-up, 0.1 nm/sec, 200 nm, mask Fig. 3-6(b)

Table 3.3: Photolithographic isolation recipe for MIT EML

Step	**Conditions**	**Time (minutes)**
Pre-bake	100°C	5:00
Spincoat OCG-PR	3000 RPM	0:30
Bake	100°C	5:00
Expose with mask	Fig. 3-6(c)	0:10
Develop in OCG-934	Rinse and check alignment	0:45
Wet etch through ZnO	5% HNO_3	0:15

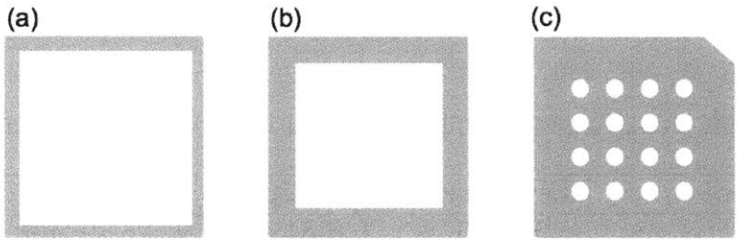

Figure 3-5: Masks used for superstrate deposition on 1×1 in^2 coupons, including (a) the ZnO layer, (b) the Cu_2O layer, and (c) the Au back contacts (cell dimensions 3.14 mm^2).

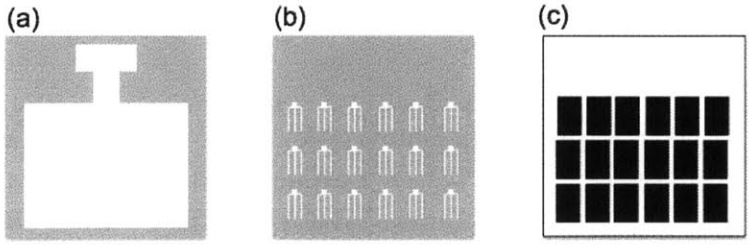

Figure 3-6: Masks used for substrate depositionon 1×1 in^2 coupons, including (a) the Au back contact, (b) the Al front finger electrodes, and (c) the photoresist exposure mask for etch isolation of cells (cell dimensions 3×5 mm^2).

Chapter 4

Device Characterization and Fitting

In this chapter, both substrate and superstrate devices are characterized to determine their structural, optical, and electronic properties.

4.1 Structural Characterization

4.1.1 X-ray Diffraction

Given the possibility of forming CuO or Cu under different deposition conditions, it is critical to confirm the existence of pure-phase Cu_2O. This may be done through x-ray diffraction, whereby diffracted x-rays can provide information about the lattice plane separation. As the x-ray incidence angle is altered, the diffracted x-ray path length in the material changes, allowing one to detect a range of plane separations present in the sample. Perfect, single-crystalline materials would yield a peak corresponding to a single lattice orientation (as well as multiples of this). Polycrystalline materials, on the other hand, will show a range of peaks based on the competing grain orientations near the surface. XRD performed on Cu_2O thin films typically detects either (111) or (200) orientations [7].

In Fig. 4-1, the XRD signal for a room-temperature sputtered film on gold is

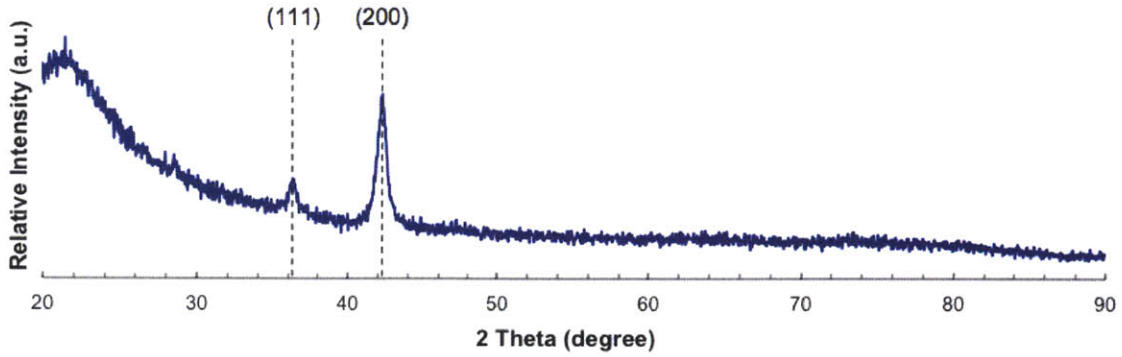

Figure 4-1: X-ray diffraction on a sputtered Cu_2O film on gold, a typical substrate material. Dominant peaks appear for the (200) and (111) orientations.

shown. Sputtered films exhibit predominately the (200) orientation, whether grown directly on quartz or on a gold film substrate. As the sputtering deposition temperature increases, the full-width-half-maximum (FWHM) of the (200) peak decreases. FWHM is an indication of the disorder of the film, and can be used to estimate grain size.

In electrochemically deposited Cu_2O thin films, the film is instead predominately (100) orientation when deposited at high pH (pH = 12.5). The XRD trace is seen in Fig. 4-2 and matches Mizuno's results [29]. There is no indication that either the (200) or (111) orientations yields better electronic transport properties. What is important, is that XRD identifies the sole presence of the Cu_2O phase in both electrodeposited and sputtered films, regardless of orientation.

4.1.2 Scanning Electron Microscopy

Once device stacks have been produced, Scanning Electron Microscopy (SEM) is a powerful tool for imaging the layer structure and confirming layer thicknesses and geometry using the higher resolution capability of electrons.

A micrograph of an electrochemically deposited Cu_2O device is presented in Fig. 4-3. The highly textured pyramidal surface is a result of the preferred (111) grain orientation. Underneath is a 200 nm thick Au film, and capping the Cu_2O is a 50 nm thick ZnS layer. Above this is a 100 nm thick Al:ZnO layer; the aluminum finger

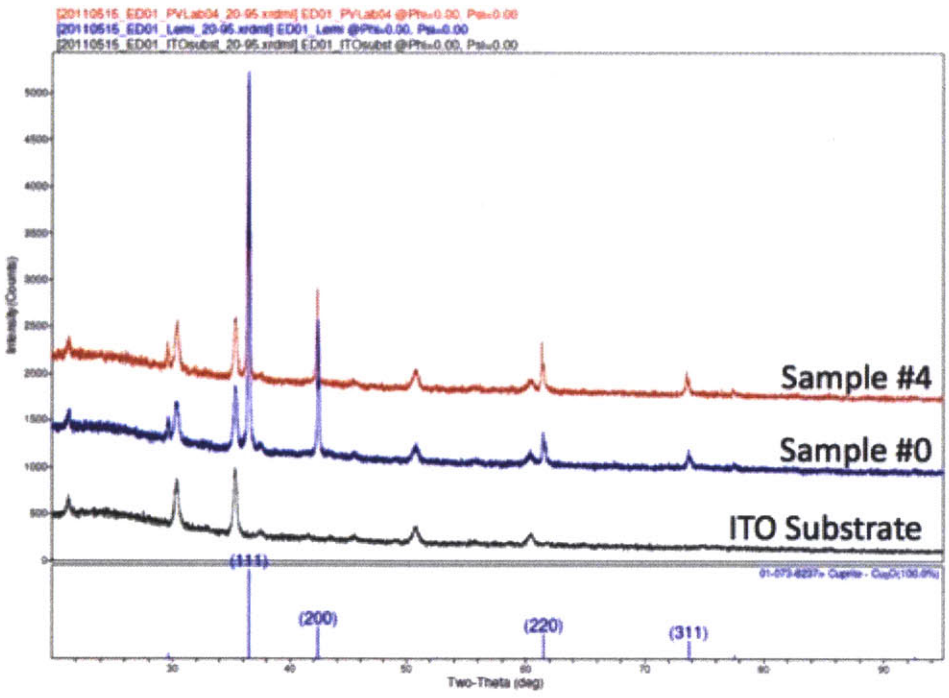

Figure 4-2: X-ray diffraction on an electrodeposited Cu_2O film on gold. Dominant peaks appear for the (111) and (200) orientations.

electrodes are not visible here. The top ZnS and ZnO layers are deposited by ALD, and result in conformal coverage of the surface texture. This micrograph is used to confirm layer thicknesses, grain sizes, and to look for structural problems including voids and pinholes through the absorber. Here, the Cu_2O exhibits a dense, columnar grain structure, with no pinholes. However, visible light micrographs taken on highly shunted devices do exhibit pinholes through the device, as seen in Fig. 4-4.

4.2 Optoelectronic Characterization

The most critical test for a solar cell is its rectification ability, determined through a dark current-voltage $I-V$ measurement. This measurement is performed using either a Keithley 4200 or Keithley 2400 Sourcemeter applying a voltage sweep (Force) and reading the output current (Measure). Typically the 3.14 mm^2 area devices require a small compliance of < 1 mA and low noise to measure nanoamps of current (time for each measurement bias is 0.2 s).

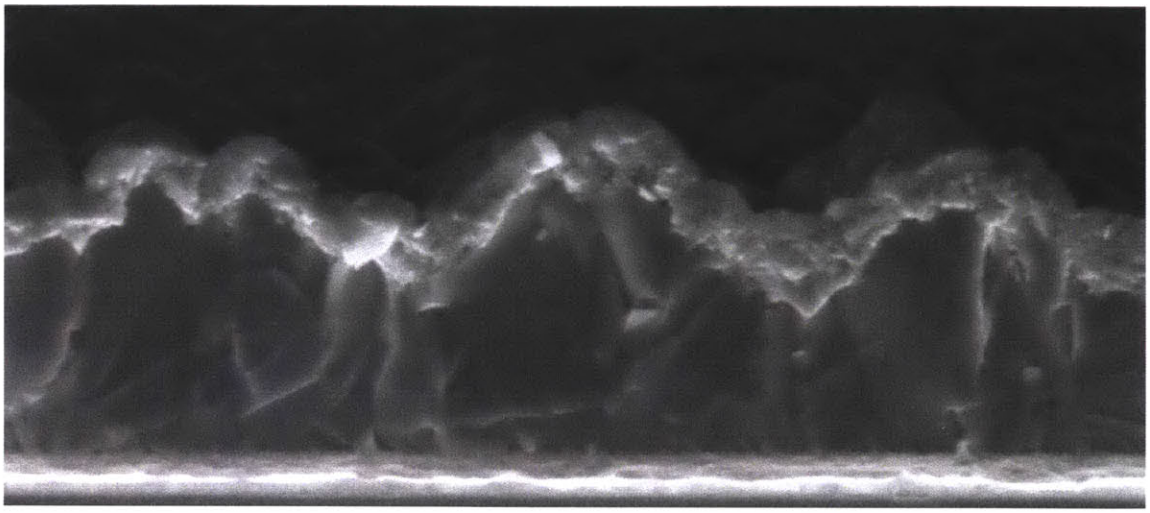

Figure 4-3: Scanning electron micrograph of an electrochemically deposited Cu_2O (2 μm) device on gold (200 nm), capped by ZnS (50 nm) and Al:ZnO (100 nm). The preferential (111) orientation results in pyramidal surface texture.

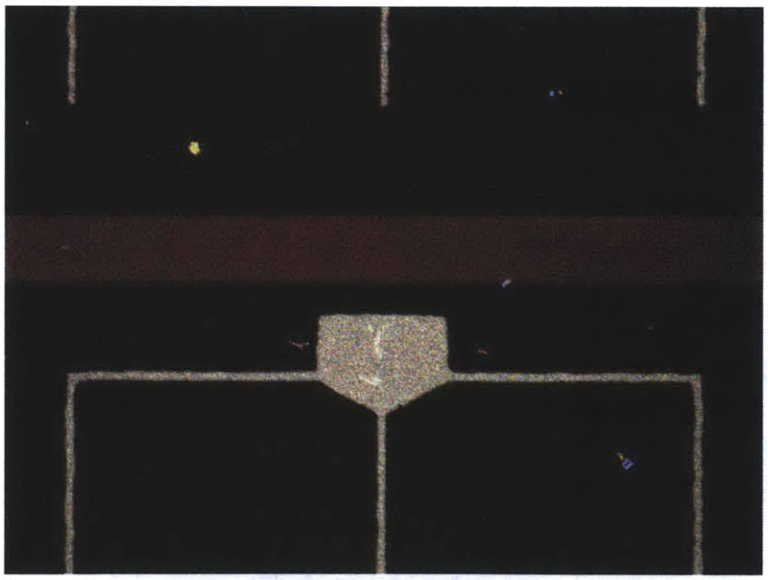

Figure 4-4: Optical microscope micrograph of an electrochemically deposited Cu_2O device on gold, showing the contact pads, finger electrodes, and isolation between neighbouring cells. Small pinholes in these devices are revealed where the gold shines through.

Measurements were performed in the dark for all devices, over the -1 to $+1$ volt range. If the devices were rectifying, those with the lowest dark current were identified. The best of these were then tested under illumination. Higher-performing illuminated devices (efficiencies $> 0.1\%$) were then subjected to external quantum efficiency measurements, and capacitance measurements as a function of voltage or frequency.

In the following chapter, high performing devices will be characterized and profiled as test cases for simulation.

4.2.1 Current vs. Voltage

During the period of August 2011 to March 2012, 76 "coupons" were processed into arrays of devices. The vast majority of these were fabricated superstrate-style on ITO, FTO, or Al:ZnO (AZO). Thus, device area was defined by a 0.0314 cm^2 circular gold electrode, 16 per coupon typically. This resulted in over 1000 testable devices. Many of these devices were not rectifying, and were often ohmic.

Figure 4-5 shows a collection of a majority of the first 200 devices tested, over 15 substrates. The most striking trend is the sheer number of ohmic $I-V$ characteristics, indicating either large amounts of shunting, or a very poor rectifying junction. Less than 10% of these devices show rectifying characteristics.

Major improvements in cleaning procedures helped increase the device yield by reducing contamination and shunting. Substrate cleaning began including ultrasonication in detergent, DI water, acetone, IPA, and DI water again. Before the ultrasonication, the surface was often scrubbed with detergent and a soft swab. Following the liquid cleaning procedures, the ITO and FTO substrates were then subjected to an oxygen plasma treatment at 50-100 W of power for at least 30 seconds. This cumulative cleaning procedure was employed for substrates 14 and 15, and resulted in over 60% of these devices producing rectifying characteristics. These cleaning procedures were adopted for future devices, greatly reducing the frequency of shunting.

Difficulties in achieving consistent properties in sputtered Cu_2O properties led to many of the ensuing devices performing very poorly, and often ohmically. Attempts

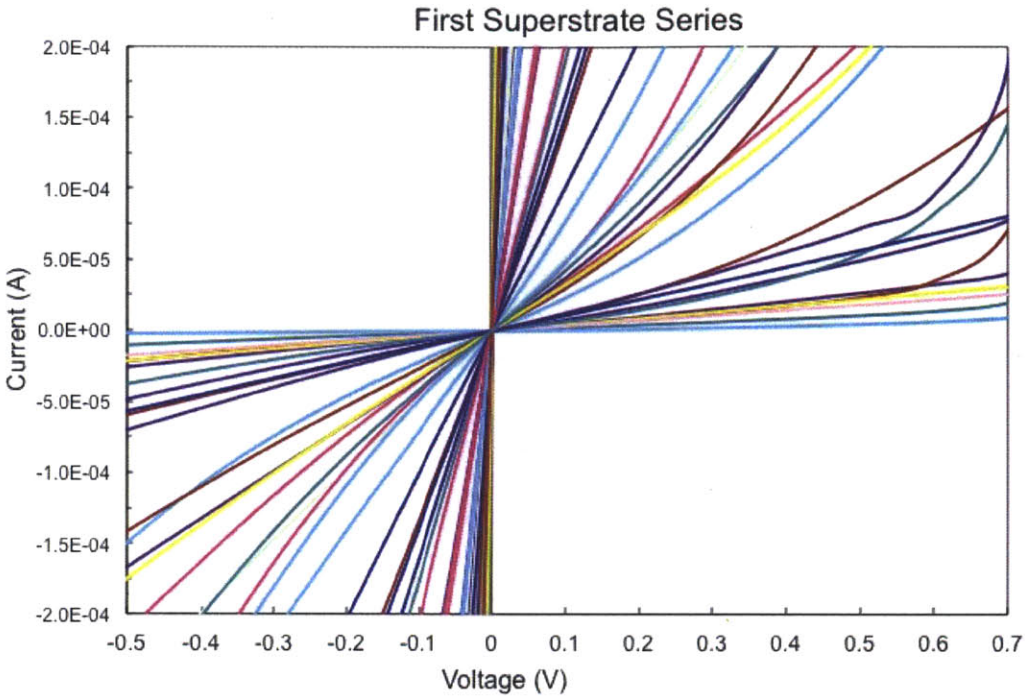

Figure 4-5: Current vs. voltage curves for the first 200 devices tested. Many of these are shunted and exhibit ohmic characteristics.

to make substrate devices with sputtered Cu_2O and ZnO also performed poorly. Aging of the copper target led to irreproducibility, and due to a lack of a consistent, high-quality sputtered Cu_2O, progress on sputtered devices slowed in early 2012.

Through this process, however, the author hypothesized that an all-sputtered device was leading to ion bombardment damage at the interface, reducing the quality of the heterojunction, the driver of charge separation. The sputtering deposition conditions were altered to use a higher chamber pressure, to reduce ion momentum and thus interfacial damage. The highest performing substrate devices were deposited with a chamber pressure of 4 mTorr, rather than the original 1.3 mTorr.

To conclude this discussion, the best-performing all-sputtered device measured was a device from coupon 14. This was deposited on ITO-coated glass (sheet resistance 7 ohm/$\square$), with the process steps outlined in Table 3.1. The $I-V$ characteristics of this cell are shown in Fig 4-6.

Table 4.1 shows the fitted device parameters for this superstrate device in the dark, which can be used to determine output current using the illuminated single-

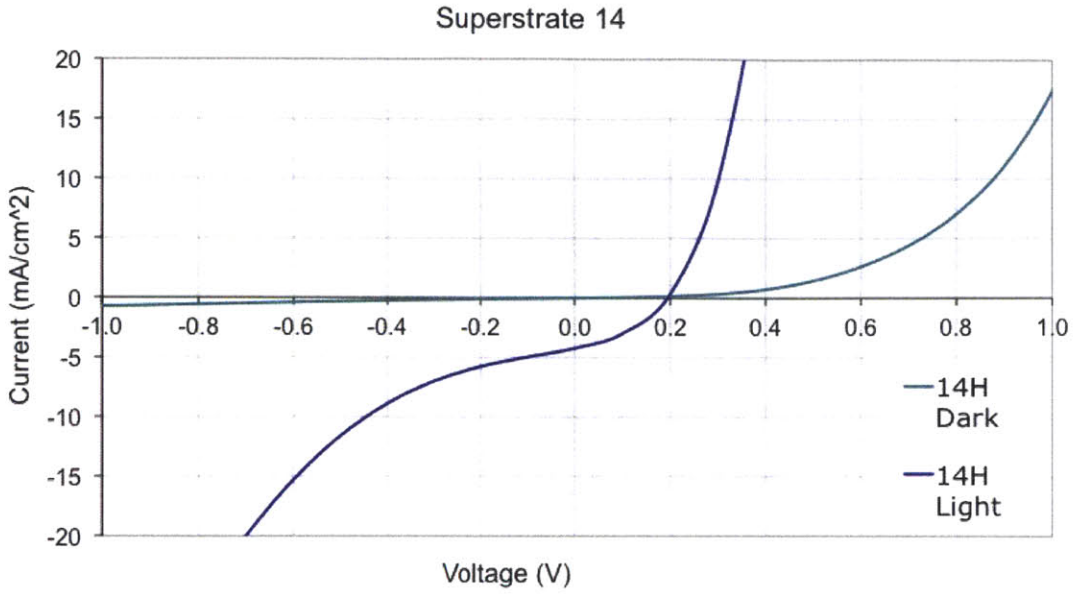

Figure 4-6: Dark and illuminated current density vs. voltage curve for the highest performing superstrate Cu_2O/ZnO device, with an efficiency of 0.3%.

diode equation, where A is the ideality factor, J_0 is the reverse saturation current, R_S is the series resistance, and R_{SH} is the shunt resistance [35]:

$$I = I_L - I_0 \exp\left(\frac{q(V + IR_S)}{Ak_BT}\right) - \frac{V + IR_S}{R_{SH}}. \tag{4.1}$$

Following these results, new device fabrication procedures were implemented, including electrochemical deposition (ECD) of the Cu_2O layer and atomic layer deposition (ALD) for the heterojunction partner materials. The first batch of substrate devices in Fig. 4-7 consisted of 72 devices, over a range of four Zn(O,S) buffer layer compositions. Approximately 50% of these exhibited shunted, ohmic characteristics.

The second batch of substrate devices in Fig. 4-8 consisted of 72 devices, again of varying Zn(O,S) compositions. Fabrication improvements were made including plasma cleaning of the substrates, thicker (2.5 μm) Cu_2O layers, and adding spacers between the masks and substrates to avoid scratching during deposition. By reducing the possibility of pinholes and shunting, nearly all of these devices were rectifying, representing the highest yield yet.

Table 4.1: Superstrate device parameters

Property	**Value**
η	0.3%
V_{OC}	0.19 V
J_{SC}	4.2 mA/cm^2
FF	0.38
J_0	6×10^{-5} A/cm^2
A	5.8
R_S	2.1 Ω·cm^2
R_{SH}	1.7×10^{3} Ω·cm^2

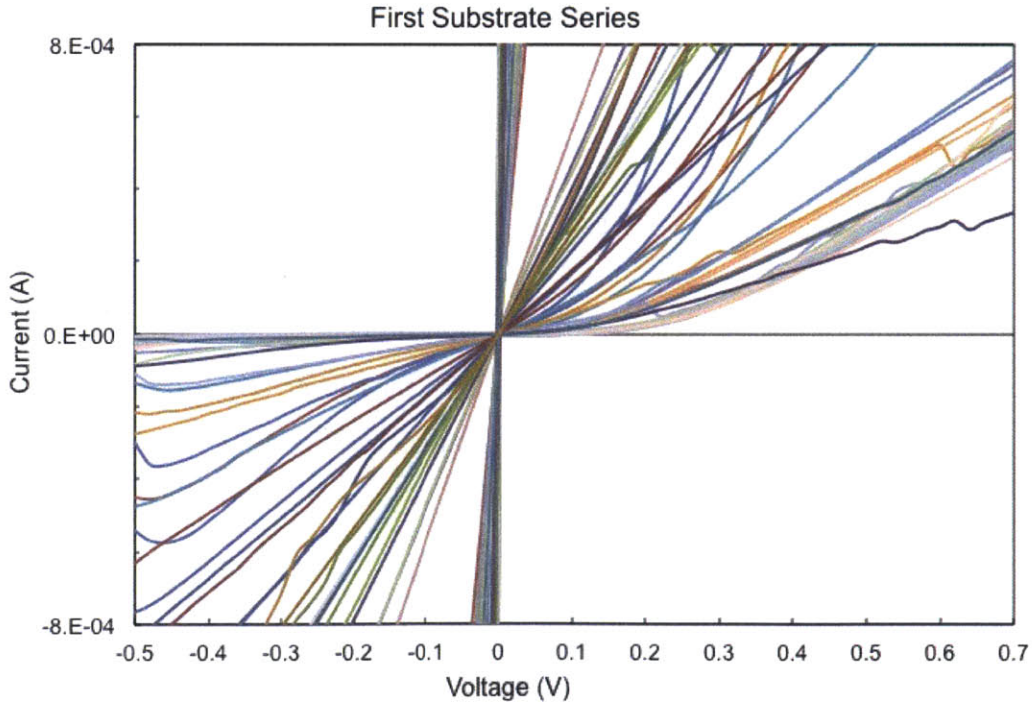

Figure 4-7: Dark current vs. voltage curves for all 72 devices produced in the first batch of substrate ECD/ALD devices.

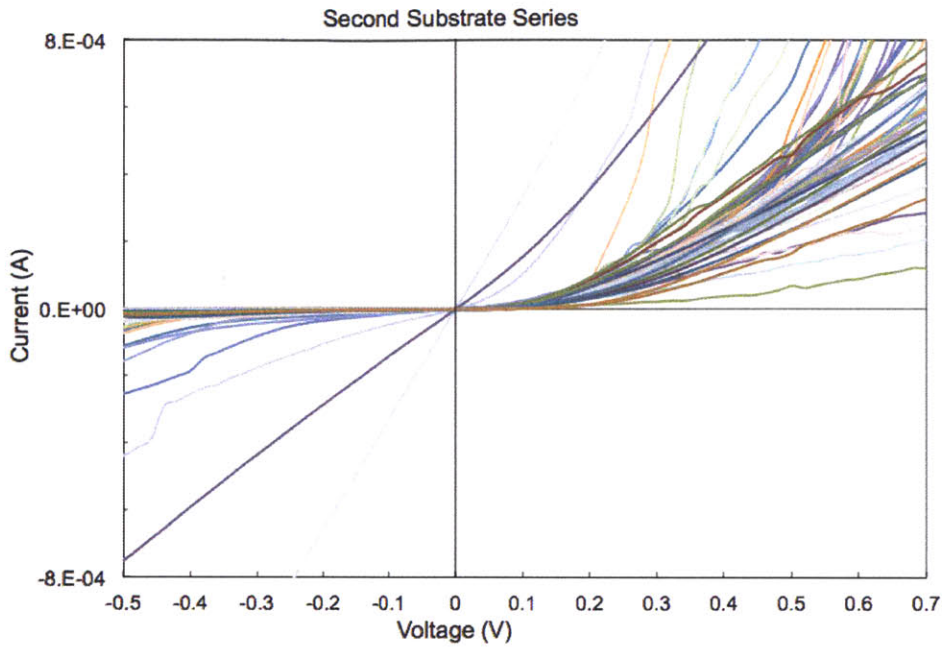

Figure 4-8: Dark current vs. voltage curves for all 72 devices produced in the second batch of substrate ECD/ALD devices.

This series of devices contained four different Zn(O,S) compositions: pure ZnO, and Zn(O,S) formed with 5:1, 6:1, and 7:1 pulse ratios of H_2O:H_2S. Raman Backscattering (RBS) was used to deduce the actual percentage of anion content that was sulfur. The best performing substrate device was found on coupon 01-008, with a pure ZnO buffer layer. This device's processing conditions are outlined in Table 3.2. The best device's characteristics are plotted in Fig. 4-9, and this device will represent the test case for simulation efforts. Top performing illuminated devices for the other buffer layer compositions are plotted as well in Fig. 4-10.

Table 4.2 shows the fitted substrate device parameters from the device in Fig. 4-9, from equation 4.1.

4.2.2 External Quantum Efficiency

The top performing devices were then subjected to quantum efficiency measurements, to determine their spectral sensitivity and diagnose generation and collection problems. These measurements were not possible with the superstate sputtered devices,

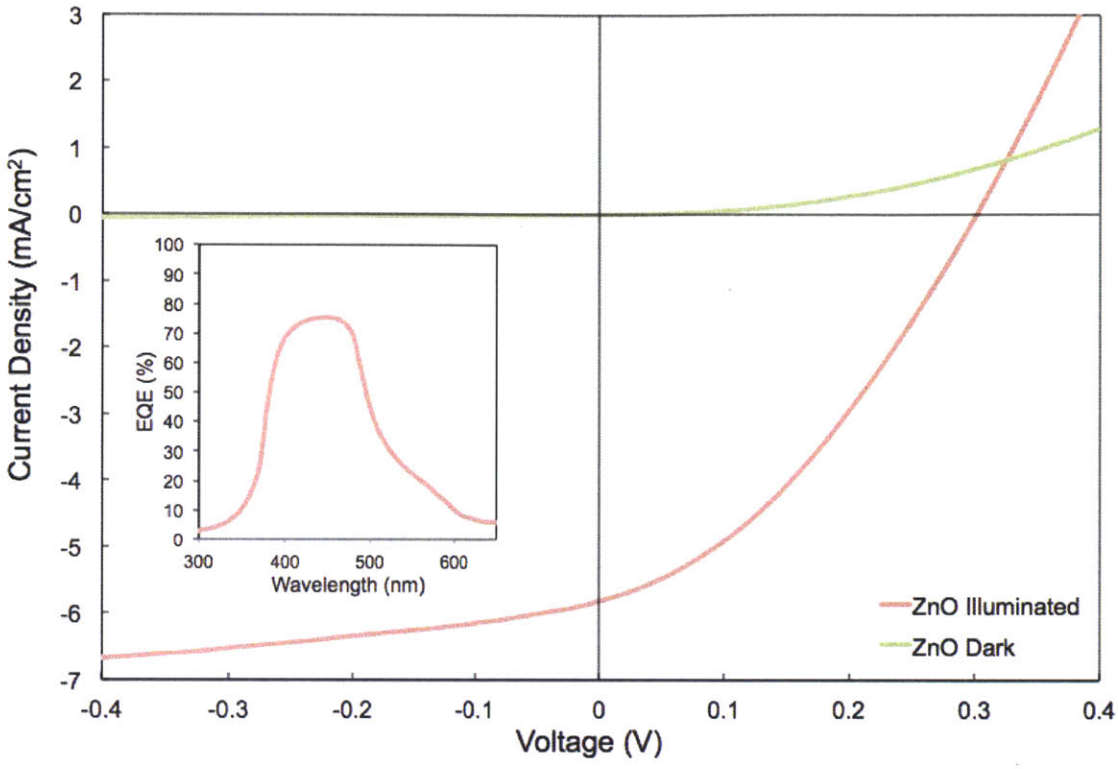

Figure 4-9: Dark and illuminated current density vs. voltage curves for 01-008, the best ECD/ALD device produced, based on a Cu_2O/ZnO heterojunction. The external quantum efficiency at zero bias is inset, yielding the same integrated J_{SC}= 5.8 mA/cm^2 as that observed in the AM1.5 $J-V$ trace.

Table 4.2: Substrate device parameters

Property	Value
η	0.62%
V_{OC}	0.3 V
J_{SC}	5.8 mA/cm^2
FF	0.36
J_0	1.5×10^{-5} A/cm^2
A	2.3
R_S	96 $\Omega\cdot$cm^2
R_{SH}	8.9×10^3 $\Omega\cdot$cm^2

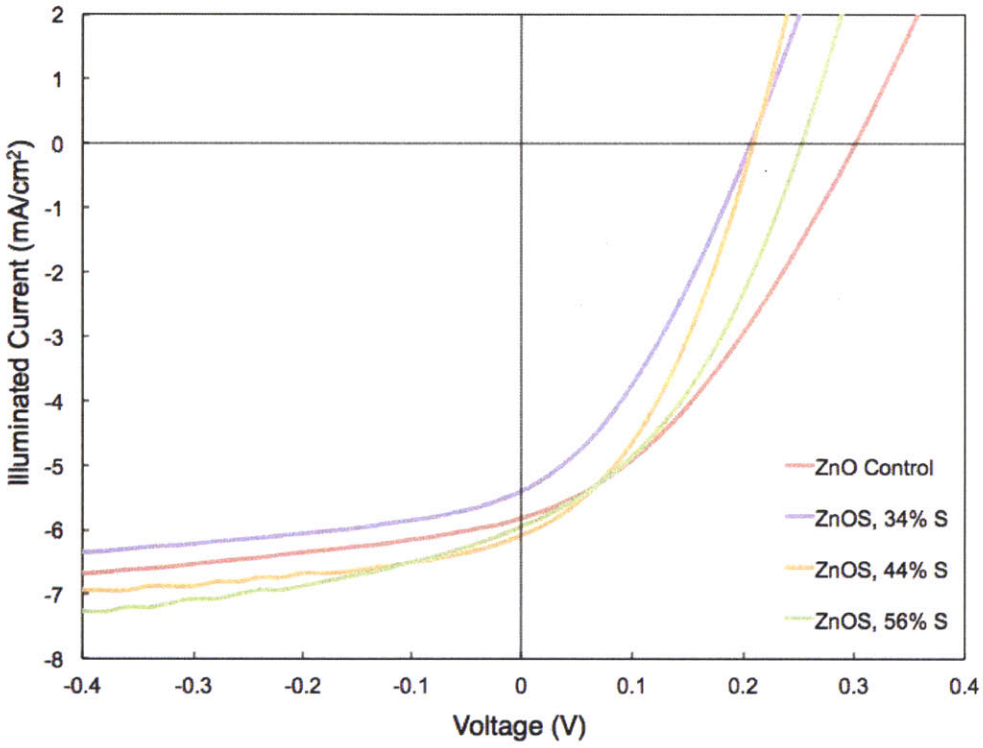

Figure 4-10: Top performing illuminated current density vs. voltage curves for each Zn(O,S) ALD buffer layer compositions on substrate devices. Performance varies predominately in the open-circuit voltage.

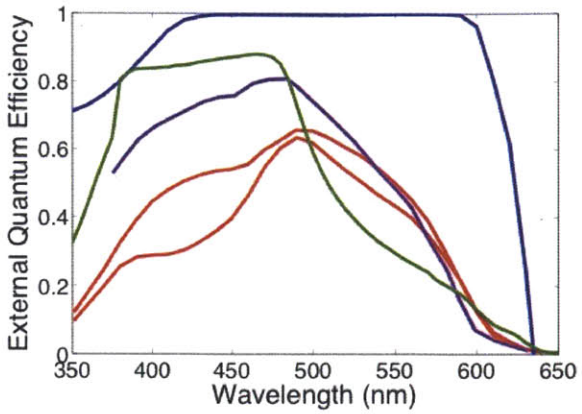

Figure 4-11: A comparison of the external quantum efficiency of literature devices, including thermally oxidized devices in (red) [11] and purple [15], as well as a thin-film device produced in the PV Lab (green) [27]. An ideal EQE spectrum for approaching the Shockley-Queisser limit is plotted in (blue).

given the small device area compared to the QE tool optical spot size.

External quantum efficiency is plotted in the inset of Fig. 4-9, for the highest efficiency substrate device. This QE curve shows a peak collection efficiency of 75% at 450 nm, dropping off near 380 nm and decaying down to the band edge (expected to be at 620 nm).

Very little quantum efficiency data is available in literature, but where possible, it has been collected into Fig. 4-11 to offer a comparison between thin-film devices and thicker oxidized foils. The thicker oxidized foils (purple, red) exhibit improved collection efficiencies at longer wavelengths over the thin film device (green) [27]. This thin film device, produced in the PV Lab at MIT, will also be used to model device parameters in the following sections.

4.2.3 Internal Quantum Efficiency

Converting external quantum efficiency (EQE) measurements to internal quantum efficiency (IQE) requires understanding the reflectance and transmittance losses at the front surface of the cell. Reflectance measurements are performed using a UV-VIS spectrophotometer, calibrating to a Spectralon reflectance standard. Direct and specular reflectance is measured by an integrating sphere.

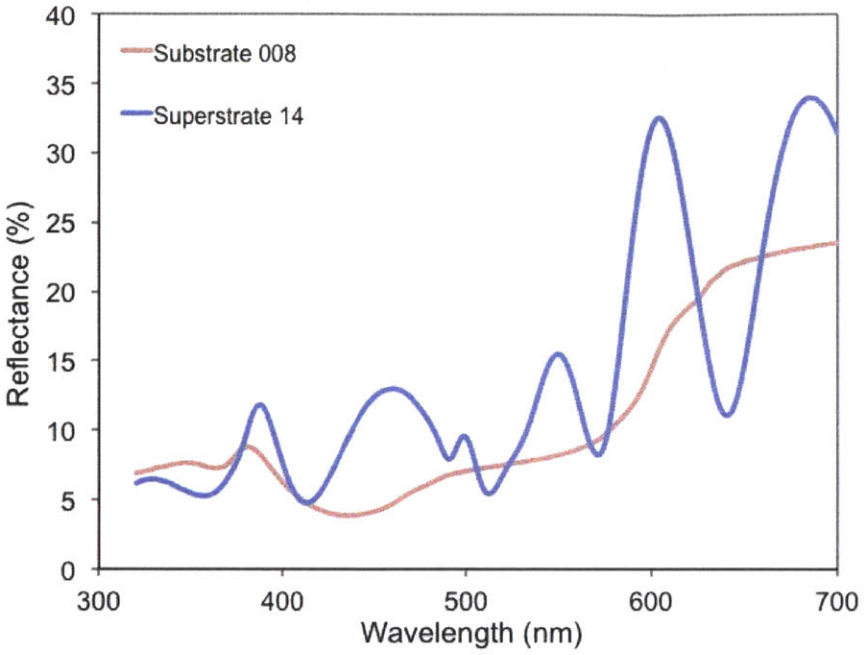

Figure 4-12: Reflectance spectra of highest performing superstrate and substrate Cu_2O devices.

The reflectance of the best substrate and superstrate devices are plotted in Fig. 4-12. In the substrate device, a combination of a higher degree of control over anti-reflection properties on the illuminated surface, as well as a high degree of surface texture, results in a lower overall reflectance.

In addition, the transmittance of the front transparent conductor may be calculated given its thickness and absorption coefficient, by:

$$T(\lambda) = \exp(-\alpha(\lambda)d). \tag{4.2}$$

The combination of the reflectance and transmittance losses allow for complete modeling of the EQE spectra. Surface recombination velocity at the interface, and bulk recombination lifetime, are fitted to the full EQE spectrum. An example of this fitting is seen in Fig. 4-13. This suggests that $\mu\tau \approx 1.1 \times 10^{-9}$ cm^2/V for electrochemically deposited Cu_2O, given $S_i = 10^3$ cm/s, and 50% back surface reflectance. For a mobility of 1 cm^2/V·s; this corresponds to a lifetime of 1.1 ns. Fitting the EQE instead with the geometric mean absorption coefficient (Fig. 2-1) gives a lifetime of 0.6 ns.

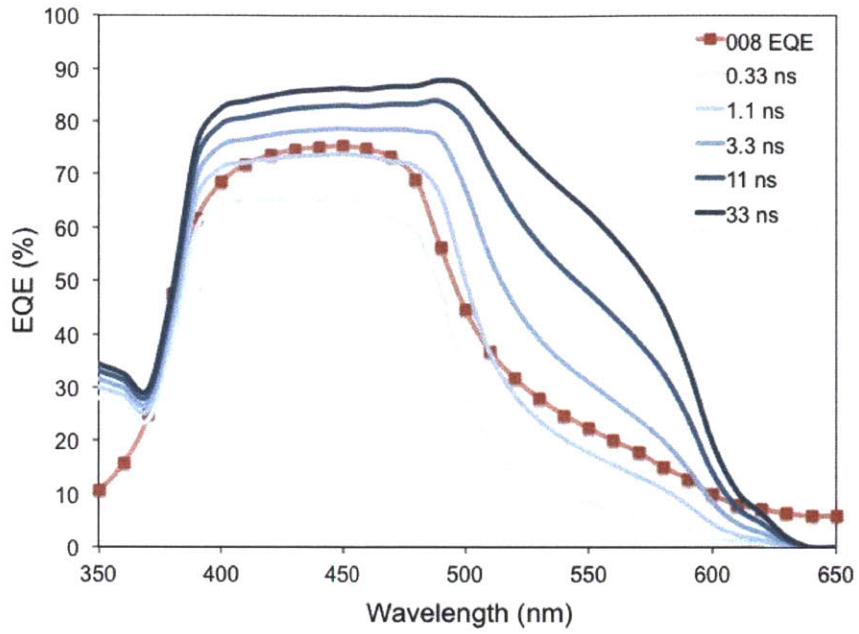

Figure 4-13: Fitting the carrier lifetime (assuming electron mobility of 1 $cm^2/V{\cdot}s$) for a 2.5 μm thick Cu_2O device in SCAPS. The fitted EQE suggests that $\mu\tau \approx 1.1 \times 10^{-9}$ cm^2/V. This results in a short-circuit current density of 5.8 mA/cm^2.

Fitting to Sopra's absorption coefficient is only possible if a highly depth-dependent defect distribution is assumed.

A similar fit was also performed for Xiang's thermally oxidized foil device, giving $\mu\tau \approx 1.7 \times 10^{-7}$ cm^2/V, and $S_i = 2.8 \times 10^5$ cm/s. This suggests improved interface properties in the present work, but that the bulk transport properties of electrochemically deposited Cu_2O are much worse than those of thermally oxidized foils.

The present fitting incorporates the minimum number of assumptions about light-trapping and defect distributions, following Occam's Razor. However, a more accurate FDTD generation model may provide a more accurate lifetime fit. The highly textured front surface and back surface reflectance should result in higher generation rates closer to the junction; thus the present lifetime fit is thought to be optimistic.

4.2.4 Capacitance Measurements

The capacitance of a thin-film photovoltaic device can reveal much about its properties, though interpretation of capacitance measurements is convoluted by the poly-

crystalline and inhomogeneous nature of these junctions. Nevertheless, the $C-V$ trace can be used to determine the junction's built-in voltage, and the $C-f$ trace can determine information about the defect levels and depletion depth of the junction. Performing these measurements as a function of temperature and/or illumination can reveal a great deal about the defect levels and distributions in the absorber.

The capacitance vs. voltage at 30 kHz is plotted for the highest performing devices in Fig. 4-14. At higher frequencies approaching MHz, the capacitance saturates at the geometric capacitance of the junction, as the filling and emptying of defect states occurs on slower time scales. This geometric capacitance C_{g} can be calculated as:

$$C_{\mathrm{g}} = \frac{\varepsilon A}{t_{\mathrm{Cu_2O}}}. \tag{4.3}$$

This results in a geometric capacitance for a 2.5 μm thick, 0.15 mm^2 area $\mathrm{Cu_2O}$ device of $C_{\mathrm{g}} = 3.7$ nF, which matches that seen in experiment at high frequencies. At lower frequencies, defects in the space charge region or at the heterojunction interface can influence the capacitance. As the cell capacitance diverges at low frequencies, it suggests a variation in the defect density across the different buffer layer compositions. Further study on the nature of these defects will be critical for determining the limiting defects in $\mathrm{Cu_2O}$ heterojunctions. In particular, performing these measurements as a function of temperature in deep-level transient spectroscopy (DLTS) could yield many answers.

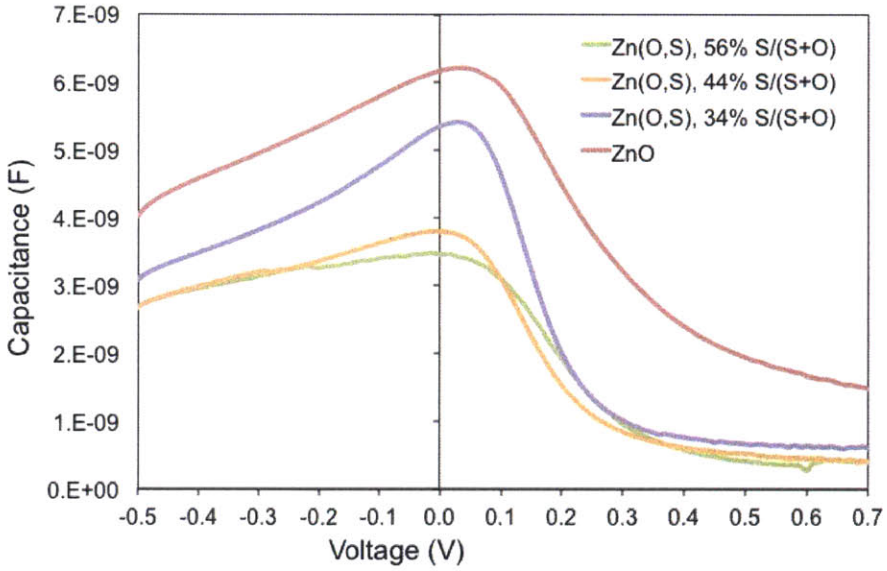

Figure 4-14: Dark capacitance vs. voltage curves for the highest-performing ECD/ALD substrate devices produced, based on Cu_2O/Zn(O,S) heterojunction.

Chapter 5

Simulating Losses and Potential Improvement

Simulation of the $I-V$ and QE curves in Chapter 4 allowed for the extraction of device and material properties. The effects of these properties on efficiency and strategies for their improvement are discussed in the present section. Determining which of these properties are intrinsic to Cu_2O, and which are capable of being engineered by material or device improvements, is critical for defining the important research questions.

5.1 Bulk Properties and Collection

In Chapter 4, the $\mu\tau$ product in the highest performing Cu_2O device was found to be 1.1×10^{-9} cm^2/V. For an expected mobility of 1 cm^2/V·s, this produces a carrier lifetime of 1.1 ns. At such low $\mu\tau$ products, the collection efficiency is limited, and the drift length is significantly less than the device thickness. However, the losses in J_{SC} are not exclusively due to low collection lengths, and can be broken down into parasitic transmittance, reflectance, and collection losses.

Fig. 5-1 shows this breakdown by loss mechanism, from a total possible photocurrent of 15.9 mA/cm^2 (AM1.5 spectrum, assuming no recombination). A vast majority of the lost photocurrent is due to the poor collection length in the bulk Cu_2O. A more

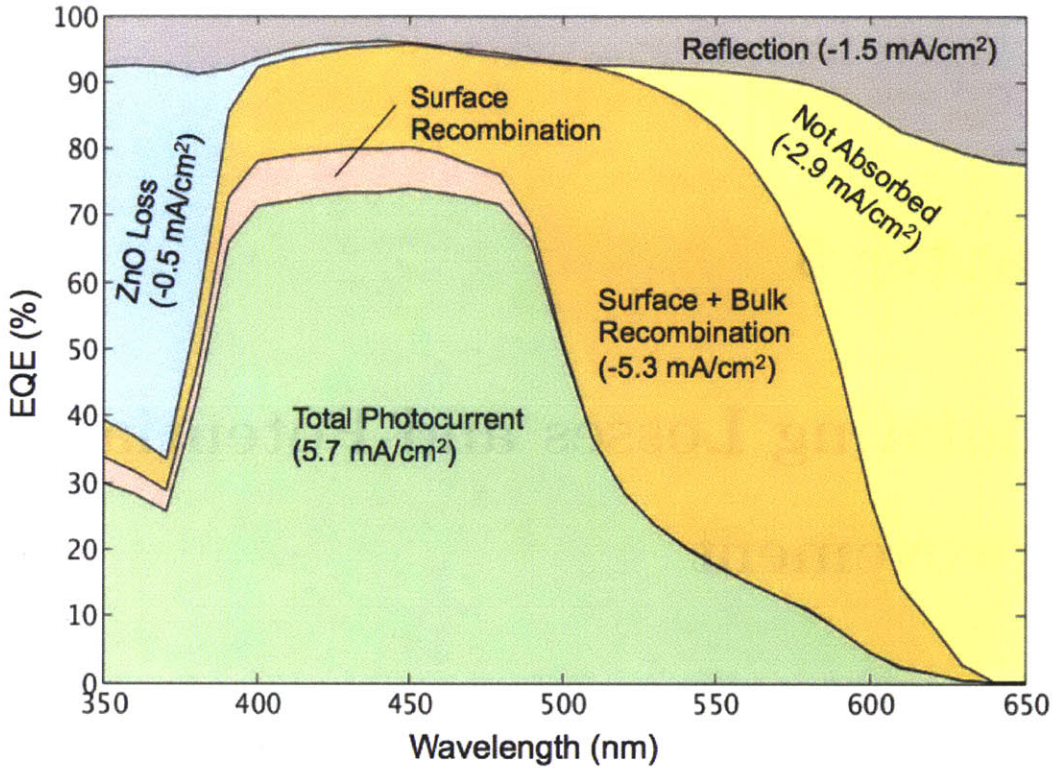

Figure 5-1: External quantum efficiency broken down by the specific loss mechanisms over all wavelengths, including optical and collection losses.

constructive picture of these losses would be to look at a plot of their effects on J_{SC}.

Firstly, the effect of Cu_2O thickness on J_{SC} is important. Assuming no reflection or transmission losses or gains, and a 1-D generation profile in Cu_2O, a simple prediction of J_{SC} as a function of layer thickness may be plotted in Fig. 5-2. Now, considering empirical reflectance losses, and absorption in a 150 nm ZnO front layer, a parasitic-loss limit to J_{SC} may be plotted for a range of layer thicknesses.

Assuming the same generation profile, one can consider the effect of changing collection profiles, or changing $\mu\tau$ product. If the layer thickness of the Cu_2O extends beyond the collection length, then additional Cu_2O thickness will not result in a higher J_{SC}. Each $\mu\tau$ product, given no light-trapping or optical engineering, exhibits a maximum J_{SC}. These successive J_{SC} maxima are also plotted in Fig. 5-2. For the present inferred $\mu\tau$ product of 1.1×10^{-9} cm^2/V, the J_{SC} saturation limit (given no internal reflection) is only 7.5 mA/cm^2, while for the $\mu\tau$ product of thermally oxidized foils (1.7×10^{-7} cm^2/V), the J_{SC} limit is 9.9 mA/cm^2. This compares well

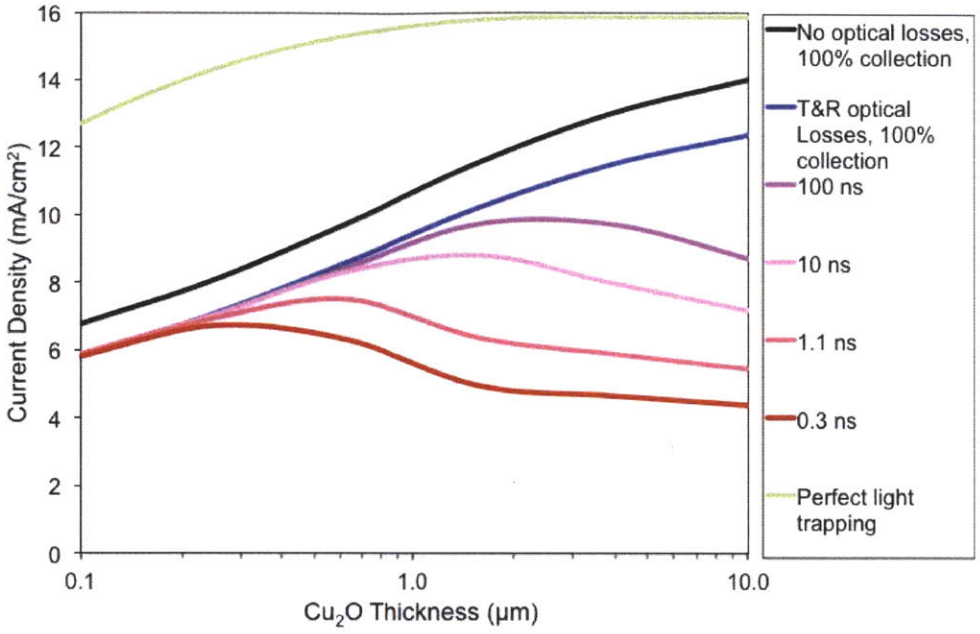

Figure 5-2: Short-circuit current under different limits, including the light-trapping limit (green) predicted by the $4n^2$ Yablonovitch limit; (black) the limit assuming no light trapping and no parasitic optical losses; (blue) the limit considering existing front reflection and window transmission losses (13.6 mA/cm^2); and lastly the limits considering the effects of transport losses. Low lifetime limits the maximum photocurrent at each thickness (with no light trapping), while higher thicknesses penalize the output current by higher series resistance. Oxidized foils with higher mobilities do not exhibit the same series resistance losses at these thicknesses.

to the highest published J_{SC} values of 10.1 mA/cm^2 [14], which are thicker and have much lower series resistance than the simulated device. In thicker devices, the penalty of series resistance eventually reduces J_{SC}. Oxidized foils with higher mobilities will not suffer from this series-resistance degradation as severely.

Lastly, there is the possibility of light trapping in the Cu_2O layer, which can greatly increase the photocurrent from a thinner layer. The Yablonovitch limit of $4n^2$ light trapping [36] is also plotted in Fig. 5-2, for 100% collection efficiency. As can be seen in this plot, trapping the maximum amount of light in a 500 nm layer can yield a J_{SC} of 15 mA/cm^2. Thus, light trapping in a thinner layer can significantly reduce the requirements for the $\mu\tau$ product by generating free electrons closer to the junction, which will be discussed further at the end of this chapter.

An important note to conclude this discussion is that other thin-film heterojunctions in the literature appear to exhibit a saturation in their maximum J_{SC}, even

at high collection efficiencies, due to inevitable transmission and reflection losses at the front window layer. Unfortunately, this fixed current loss makes up a larger percentage of the maximum photocurrent for a wider bandgap solar cell, so avoiding these parasitic losses becomes significantly more important for Cu_2O, where current is already scarce. The use of wider bandgap window layers and well-designed anti-reflection coatings will be critical for Cu_2O, but there will be a fundamental upper limit that lies below the expected Shockley-Queisser photocurrent limit, between 13-14 mA/cm^2 rather than 15-16 mA/cm^2, if front reflection and window absorption are taken into account.

Interestingly, the difference in $\mu\tau$ products between thermally oxidized and ECD Cu_2O appears to be predominantly in the mobility, which is different by two orders of magnitude (hole mobilities of 1 cm^2/V·s in ECD films vs. 100 cm^2/V·s in foils). In thin-film sputtered cuprous oxide, this mobility was found to be limited by ionized impurities, suggesting that a path forward for J_{SC} improvement would be to reduce the point defect density (and increase grain size) through thermal annealing treatments. Such an anneal would be limited by possible delamination from the substrate, and would be have to be done under very low oxygen partial pressures to avoid formation of CuO. However, this analysis suggests that almost all of the difference in $\mu\tau$ between ECD films and thermally oxidized foils is in the mobility, and not in the lifetime.

This suggests that long-term, improving $\mu\tau$ may require focusing on what is limiting lifetime in the films, through a combination of experimental and computational techniques. If these defects are extrinsic, source material purity will become critical. Alternatively, chemical treatments can be used to passivate defects, which could increase lifetime and/or mobility. Hydrogen plasma and dissolved potassium cyanide have both been used to chemically treat Cu_2O, and have resulted in improvements in the photoluminescence spectra intensity [37][38]. This could be a promising path forward.

A final material improvement strategy could be to combine the benefits of thermally oxidized mobilities, with the thickness (better fill-factor and light-trapping opportunities) of thin-film devices. This would involve depositing a thin film of copper

metal, lifting it off a substrate (possibly by using a soluble rocksalt substrate [39]), and then thermally oxidizing. Alternatively, a thicker foil could be oxidized as normal, then wet-etched with nitric acid and/or hydrochloric acid down to a thin film. These methods may yield higher efficiencies in thin-film devices, but are questionable in their manufacturing scalability unless further process innovation occurs.

5.2 Open-Circuit Voltage

Bulk recombination can limit V_{OC} by increasing the reverse saturation current into the bulk [15]:

$$V_{OC} = \frac{k_B T}{q} \ln\left(\frac{J_{ph} L_{diff,n} N_A}{q D_n n_i^2}\right). \tag{5.1}$$

Given $\mu\tau = 1.1 \times 10^{-9}\text{cm}^2/\text{V}$, this results in an estimated bulk-limited V_{OC} of 1.3 V. Voltages well below this suggest that the V_{OC} is interface-limited instead, and in particular by the conduction band offset.

The majority of the deficit in V_{OC}, and in turn the FF and overall efficiency, comes from the poor conduction band alignment between Cu_2O and partner n-type materials. In Fig. 5-3, the V_{OC} is plotted as a function of the conduction band offset ΔE_C and the surface recombination velocity. Over a wide range, the V_{OC} varies linearly with ΔE_C, until it saturates at a recombination-limited maximum. Improvements in bulk lifetime and surface recombination velocity would push this limit closer to the 1.5 volt Shockley-Queisser maximum. Recent photoelectron spectroscopy measurements (UPS and XPS) determined this conduction band offset between electrochemically deposited Cu_2O and ALD ZnO to be -1.5 eV $\pm$ 0.2 eV [27]. This offset may account entirely for the low V_{OC}, with a minimal contribution from surface recombination velocity based on simulation.

Future cells will require a higher built-in voltage in the absorber V_{jp}, in order to achieve higher V_{OC}. This necessitates finding a metal or n-type semiconductor ($n > 10^{18}$ cm^{-3}) with a work function that aligns within $\pm$0.3 eV of the Cu_2O conduction band. Literature devices using different n-type materials provide some direction, showing a significant improvement of the V_{OC} by improving the conduction

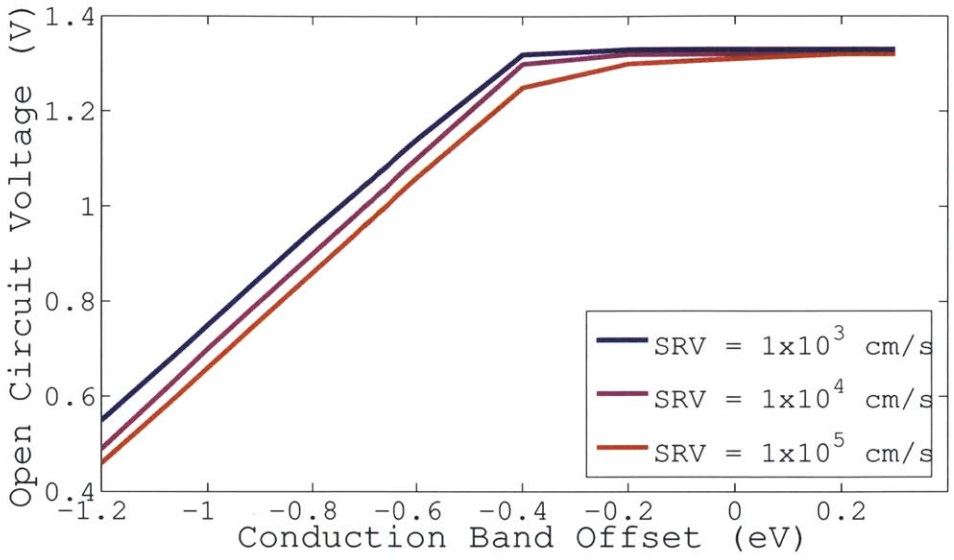

Figure 5-3: The effect of conduction band offset and surface recombination velocity on the open-circuit voltage of a thin-film Cu_2O cell.

band alignment, as seen in Fig. 5-4. A good predictive model for conduction band offset would greatly accelerate the discovery of better n-type materials.

5.2.1 Predicting Conduction Band Alignment

The interfaces between semiconductors have historically been well studied, but poorly understood. Over seven decades of literature exist attempting to predict the conduction and valence band alignments between semiconductors, as well as alignments to the work functions of metals. Many models have only proven to be accurate in limited cases, *e.g.*, just III-V semiconductors, or just between silicon and metal oxides. However, most models have converged on a common description, which holds that alignment occurs according to the energy relative to vacuum, plus an additional surface dipole or charge that offsets the bands in either direction. The measurement of electron affinity or ionization potential allows for easy prediction of the bulk component of band alignment, but understanding the interface dipole is more difficult.

For metal-semiconductor (M-S) interfaces, Schottky and Mott [40] initially proposed that the work function of the metal and semiconductor (electrochemical poten-

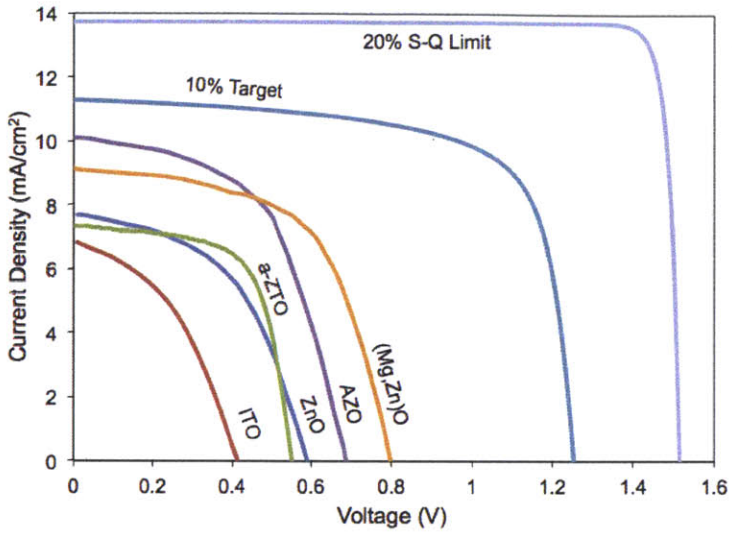

Figure 5-4: The effect of conduction band offset can be seen in literature devices, as the open-circuit voltage changes for different n-type materials. The record V_{OC} is seen with a (Mg,Zn)O (10% Mg) alloy [14]. Other cells include ZnO and ITO n-type layers [11], AZO (with a ZnO buffer) [12], and a similar electrochemical device with an amorphous zinc tin oxide (aZTO buffer layer) [27]. Possible $J-V$ curves for a 10% or 20% efficient device are plotted as well.

tial relative to vacuum) would determine the barrier height $\phi_{b,p}$ on a p-type material:

$$\phi_{b,p} = \chi_s + E_{g,s} - \Phi_m, \tag{5.2}$$

where χ_s is the electron affinity of the semiconductor, $E_{g,s}$ is the bandgap, and Φ_m is the work function of the metal. Bardeen [41] suggested instead that the metal work function aligned with the semiconductor's charge neutrality level (CNL), Φ_s. The CNL is the energy at which states in the gap change from donor-type to acceptor-type character. Many subsequent theories including Metal Induced Gap States (MIGS) [42], and Defect Induced Gap States (DIGS) [43] developed this into a combined model, in which alignment to electron affinity and charge neutrality level are governed by a pinning factor, S:

$$\phi_{b,p} = S(\Phi_s - \Phi_m) + (\chi_s + E_{g,s} - \Phi_s). \tag{5.3}$$

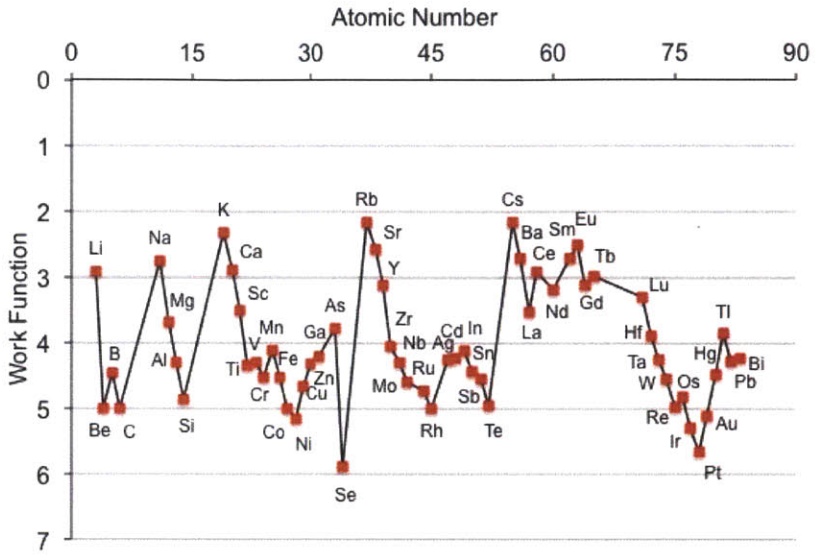

Figure 5-5: The work function of a wide range of metals, for determining Schottky barrier heights. After [46].

Tersoff [44] derived an expression for S:

$$S = \frac{1}{1 + \frac{q^2 N \delta}{\epsilon_o}}, \tag{5.4}$$

where N is the density of states, and δ is their penetration depth into the semiconductor. When $S = 1$, there is no interface dipole (Schottky Limit), and when $S = 0$, alignment is by CNL (Bardeen Limit). Later, an empirical correlation was established between S and the optical dielectric constant ϵ_∞:

$$S = \frac{1}{1 + 0.1(\epsilon_\infty - 1)^2}. \tag{5.5}$$

Robertson determined that the CNL of Cu_2O was 0.8 eV above the valence band [45], which is 4.4 eV below vacuum level assuming an electron affinity and bandgap of 3.2 eV and 2.0 eV respectively. In addition, given the Cu_2O optical dielectric constant of 6.46, this gives a pinning parameter of $S = 0.25$. Taking the work functions of a wide range of metals [46], the p-type barrier height can now be predicted.

In Fig. 5-5, a wide range of available metal work functions is plotted. Yet, Fig. 5-6 shows that due to Fermi-level pinning at the CNL, actual barrier heights

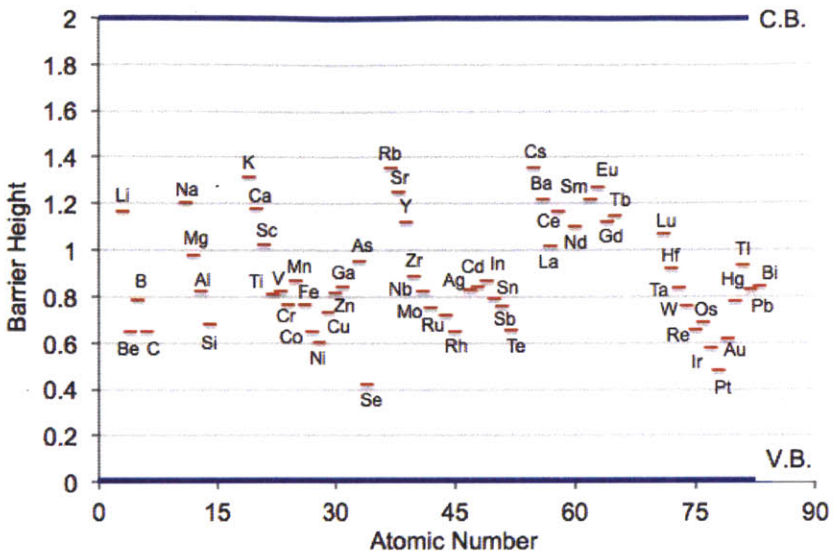

Figure 5-6: Calculated Schottky barrier heights of a wide range of metals on Cu_2O, relative to the valence band energy.

are constrained to a small energy range, midgap. Indeed, all measured Schottky barrier heights have been approximately 0.65-0.9 eV, independent of the metal [47], suggesting that this pinning effect impacts the maximum barrier height, and as a result the maximum open-circuit voltage of a Schottky structure on Cu_2O.

This pinning, however, can be overcome by the introduction of a thin dielectric layer between the metal and Cu_2O, as demonstrated by Tersoff [44]. A layer thin enough to allow tunneling, but thick enough to shield the metal's wavefunction from penetrating the semiconductor, can un-pin the Fermi energy and allow for a wider range of tunability. This thin layer, with a lower optical dielectric constant, would approach the Schottky alignment as opposed to Bardeen's pinning alignment.

A more likely strategy for improved junction properties is to form a heterojunction with more optimal conduction band alignment to Cu_2O. This alignment also deviates from the simple electron affinity alignment due to CNL pinning; here the conduction band offset between semiconductors A and B is:

$$\Delta E_C = (\chi_A - \chi_B) + (S_{A,B} - 1)(\Phi_{s,A} - \Phi_{s,B}). \tag{5.6}$$

Here, the pinning factor is determined by the optical dielectric constants of both

materials:

$$S_{A,B} = \frac{1}{1 + 0.1\left(\frac{(\epsilon_{\infty,A}-1)^2(\epsilon_{\infty,B}-1)^2}{(\epsilon_{\infty,A}-1)^2+(\epsilon_{\infty,B}-1)^2}\right)}. \tag{5.7}$$

Given the utility of semiconductor-insulator (SI) and semiconductor-semiconductor (SS) junctions, it is important to collect data to predict the alignment at these interfaces. The electron affinity, bandgap, charge neutrality, and dielectric constant for a number of compounds has been collected by Robertson *et al.* [48][49][45][50]. This data is accumulated in Table 5.1, and used to calculate the conduction band offset by equations 5.6 and 5.7.

Table 5.1 suggests several possible candidates for improved conduction band alignment. These include both wide-gap conductors, and insulating layers (used for tunneling MIS or SIS structures). Promising insulating layers include Al_2O_3, Ga_2O_3, HfO_2, ZrO_2, Ta_2O_5, or $Pb(Ti,Zr)O_3$, among others. The perovskite class of materials typically exhibits ferroelectricity, an interesting property that has been shown to have unique rectification properties [55], but they often have very poor conductivity. In an MIS or SIS structure, on a *p*-type absorber, these insulating layers would also benefit from having a positive fixed charge as a result of anion vacancies—this fixed charge would lead to improved inversion in the Cu_2O and an increased barrier height.

More importantly though, for a material to set a true *p-n* heterojunction with Cu_2O, it must be possible to dope it in excess of 10^{18} cm^{-3} electrons. This means that the bandgap must be around 3-4 eV, with no compensating native acceptors like those found in Cu_2O. The most promising candidates in this class include ZnS, ZnO (alloyed with Mg), GaN (alloyed with Al), and $SrTiO_3$. GaN and $SrTiO_3$ may be heavily doped *n*-type, but can not be deposited on Cu_2O in the substrate configuration due to high deposition temperature and power that would damage the Cu_2O and junction.

Thus, the two most promising heterojunction candidates appear to be ZnS and $Mg_xZn_{1-x}O$. In $Mg_xZn_{1-x}O$, Mg incorporation can reach $x = 0.3$ before entering an immiscibility gap, then forming a rocksalt phase. At this concentration, the bandgap grows to 4.0 eV, 90% of which is due to conduction band movement [56]. This could

Table 5.1: Semiconductor conduction band alignment on Cu_2O

Material	E_g (eV)	χ (eV)	Φ_s (eV)	ε_∞	$\Delta E_{C,calc}$ (eV)	$\Delta E_{C,exp}$ (eV)
Al_2O_3	8.8	2.5	5.8	3.4	1.6	
AlAs	2.15	3.50	4.73	8.2	-0.1	
AlN	6.2	0.6	4	4.8	2.4	
AlP	2.45	2.8	3.95	7.5	0.1	
AlSb	1.61	3.6	4.81	10.24	-0.1	
$BaZrO_3$	5.3	2.5	5.1	4	1.0	
CdS	2.42	4.5	4.99	5.3	-1.0	
CdSe	1.71	4.95	5.13	6.3	-1.3	
CdTe	1.48	4.4	4.76	7.1	-1.0	
$CuAlO_2$	3	2	4.2	6	1.1	
Ga_2O_3	4.8	3.5	5.5	4.2	0.2	
GaAs	1.52	4.15	5.12	10.86	-0.5	
GaN	3.3	3.3	4.3	5.2	-0.2	-0.23 [16]
GaP	2.3	3.2	4.7	9.11	0.2	
GaSb	0.75	4.06	4.75	14.5	-0.6	
Ge	0.66	4.0	4.61	16	-0.7	
HfO_2	6	2.5	4.8	4	0.9	
$HfSiO_4$	6	2.5	4.9	3.8	0.9	
InAs	0.35	5.06	4.91	12.37	-1.5	
InN	0.7	5.8	4.63	8.4	-2.5	
InP	1.34	4.38	5.12	10.9	-0.7	
La_2O_3	6	2	5.6	4	1.7	
$PbTiO_3$	3.4	3.5	5	6.25	0.1	
$PbZrO_3$	3.7	3.2	4.3	4.8	-0.1	
Si	1.12	4.05	4.87	12	-0.5	
Si_3N_4	5.1	2.1	4.6	3.8	1.2	
SiO_2	8.4	1	4.9	3.5	2.4	
SnO_2	3.8	4.7	4.4	4	-1.5	
$SrTiO_3$	3.3	3.9	4.6	6.1	-0.6	
Ta_2O_5	4.2	3.3	4.2	4.84	-0.2	
TiO_2	3.05	3.9	4.75	7.8	-0.5	-0.74 [51]
Y_2O_3	6	2	5.6	4.4	1.8	
ZnO	3.3	4.4	4.42	3.75	-1.2	-1.5–-1.0 [31][52][27]
ZnS	3.6	3.9	5.4	5	-0.2	
ZnSe	2.8	4.09	5.39	5.7	-0.3	
ZrO_2	5.8	2.5	4.7	4.8	0.9	
$ZrSiO_4$	6	2.5	4.9	3.8	0.9	
In_2O_3	2.6					-0.83 [53]
ITO	2.9					-1.7–-1.2 [54]

theoretically yield a conduction band offset of ≈-0.5eV, a substantial improvement over ZnO. Doping densities of $n > 10^{20}$ cm^{-3} have been achieved at 30% Mg incorporation by Ga doping, making it a promising candidate [56]. ZnS, as well, shows a theoretical conduction band alignment of -0.2 eV. Doping with halogens such as iodine has yielded $n > 10^{18}$ cm^{-3} [57].

It's very important to note that the success of these two materials as an emitter is dependent upon high doping density, and good interface chemical and structural quality. If the buffer layer is too thin or too lowly doped, it will not have sufficient fixed charge to support a *p*-*n* junction, and will be depleted of electrons by the neighbouring TCO or front contact. In this case, the neighbouring TCO or front contact will set the built-in potential, not the (Mg,Zn)O or ZnS layer. The design criteria is therefore that the layer thickness exceeds its depletion depth:

$$d_{\mathrm{n}} > W_{\mathrm{n}} = \left(\frac{2\varepsilon_{\mathrm{r,n}}\varepsilon_0 V_{\mathrm{jn}}}{qN_{\mathrm{D}}}\right)^{1/2} \tag{5.8}$$

$$V_{\mathrm{jn}} = V_{\mathrm{bi}}\left(\frac{\varepsilon_{\mathrm{r,p}}N_{\mathrm{A}}}{\varepsilon_{\mathrm{r,p}}N_{\mathrm{A}} + \varepsilon_{\mathrm{r,n}}N_{\mathrm{D}}}\right). \tag{5.9}$$

Full improvement in efficiency with conduction band alignment is not achieved until the layer is thick enough and sufficiently *n*-doped.

While the conduction band alignment is critical, it is not the only important interfacial property. The layers must also be chemically compatible, thus the cation or anion displacement reactions between Cu_2O and the partner material must be unfavourable thermodynamically or kinetically. This makes the oxides and nitrides a promising class of materials, given their stability. In addition, the ability to resist diffusion of copper is of high interest. Here, Ta_2O_5 and other early transition metal oxides and nitrides have been explored as copper diffusion barriers [58], and could be promising.

Structurally, the possibility of lattice matching is ideal, as this results in fewer defects and a lower density of interface states. These interface states are important for mitigating surface recombination velocity at the interface. Lattice matching to Cu_2O's unique cubic structure may be possible, but a more promising route could

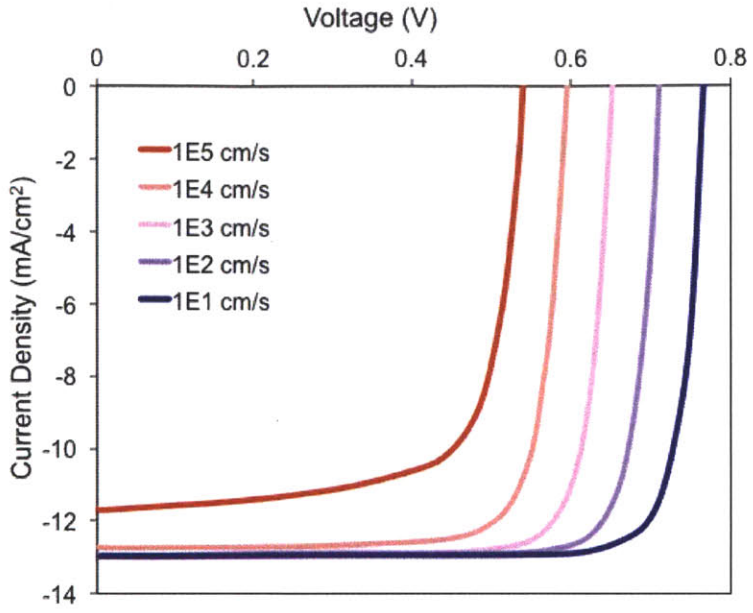

Figure 5-7: The effect of changing the interface state density and/or capture cross section at the heterojunction interface. Curves reflect varying surface recombination velocity [cm/s] at the heterojunction interface. Higher surface recombination velocities result in a lower V_{OC}.

be to pursue amorphous materials. Amorphous materials, and especially those with less directional bonding, can accommodate more disorder at the interface and tie up dangling bonds, a primary source of midgap defects at the interface. Amorphous deposition may also help reduce surface damage that accompanies sputtering and pulsed laser deposition. Again, the improvement in conduction band alignment can be completely washed out if the density of interfacial defects is high, as seen in Fig. 5-7. The effect of surface recombination velocity is captured in the following expression derived for Cu_2S/CdS junctions [59]:

$$qV_{OC} = (E_{g,Cu_2O} - \Delta E_C) + k_B T \ln(J_{SC}) - k_B T \ln(qN_{C,n}S_i) - k_B T \ln(A_j/A_\perp), \quad (5.10)$$

where $N_{C,n}$ is the conduction band density of states in the n-type material, and A_j and $A_\perp$ are the junction surface area and projected area respectively. Present devices exhibit $S_i < 10^4$ cm/s.

Amorphous materials also exhibit unexpected changes in band positions. Recent work by Lee *et al.* suggests that amorphous zinc tin oxide (a-ZTO) shows an increase

in conduction band energy over that of both crystalline ZnO and SnO_2 alone [27].

5.2.2 Effect on Fill-Factor

An improvement in V_{OC} can also improve FF, as the two are linked. For a $V_{OC} >$ 0.25 V at room temperature and typical ideality factors of 1-2, the following empirical relationship has been derived:

$$FF = \frac{v_{OC} - \ln(v_{OC} + 0.72)}{v_{OC} + 1} \tag{5.11}$$

$$v_{OC} = \frac{q}{nk_BT} V_{OC}. \tag{5.12}$$

This relationship may still be considered appropriate to within 5% for such low-performing cells. For the highest performing substrate device with an ideality factor of 2.3 and V_{OC} = 0.3 V, this would predict a fill factor of 0.54. The actual fill factor of 0.36 is lower due primarily to the high series resistance of these devices at 96 $\Omega \cdot cm^2$. This is in part due to poor aluminum finger deposition, which can yield high resistivity front contacts, in combination with a thin TCO layer deposited by ALD (sheet resistance $\approx$ 100 Ω/square). The series resistance contribution from the bulk of the Cu_2O, with a resistivity of 6×10^4 $\Omega \cdot$cm, is approximately 100 Ω (15 $\Omega \cdot cm^2$).

Improving bulk conductivity in each layer, as well as increasing the TCO thickness, could help reduce the series resistance significantly, and in tandem with an increase in V_{OC}, could result in significantly higher fill factors.

5.2.3 Effect on Quantum Efficiency

In addition to improvements in V_{OC}, better conduction band alignment also results in a lower work function in the n-type layer, and thus a larger built-in potential in the junction. This built-in field depletes the Cu_2O further and results in a higher collection efficiency by enhancing diffusion with drift collection. This effect is summarized in Fig. 5-8, with the depletion depth varying as a function of conduction band offset and n-type layer doping density. Thus, an improved conduction band

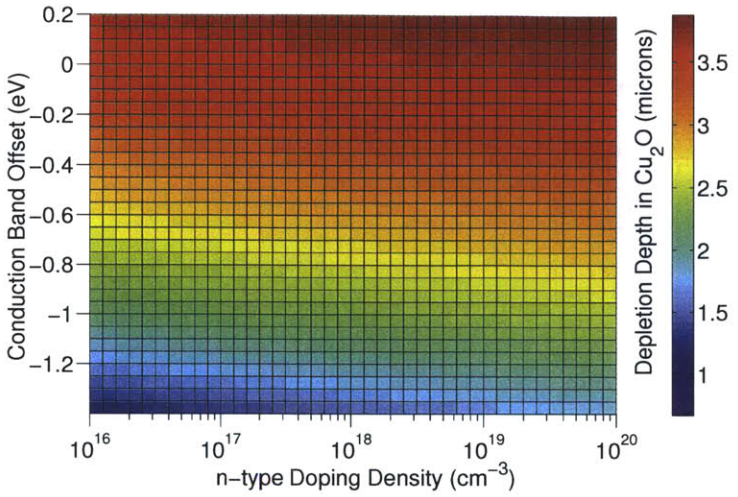

Figure 5-8: The effect of conduction band offset and doping density on the depletion depth of a Cu_2O layer with acceptor density $N_A = 10^{14}$ cm^{-3}.

offset can improve J_{SC}. This enhancement in current will not be as strong, however, at operating conditions, as the cell is in forward bias.

5.3 Loss Analysis

A full loss analysis may conducted by looking at the percentage losses in J_{SC}, V_{OC}, and FF from their Shockley-Queisser limits. This is captured in Table 5.2, demonstrating that bulk $\mu\tau$ and heterojunction ΔE_C are by far the predominant loss mechanisms in these Cu_2O cells. Fortunately, this loss analysis suggests a very clear path towards achieving 10% efficient devices.

5.3.1 Reaching 10%

Literature devices made with thermally oxidized foils have achieved short-circuit currents of 10.1 mA/cm^2, thanks in large part to a higher mobility and a thicker absorber layer. However, the present loss analysis suggests that, even without light-trapping, collecting 100% of the light absorbed in a 2.5 μm layer could push thin film photocurrents to 11 mA/cm^2. This will necessitate a two order of magnitude improvement in bulk $\mu\tau$, and even then, improved light trapping in this thin-film absorber will be

Table 5.2: Efficiency loss breakdown of a Cu_2O cell

J_{SC}	(mA/cm^2)	V_{OC}	(V)	FF	
Maximum	**15.9**	Maximum	**1.5**	Maximum	**0.92**
Reflection	-1.5 (-9%)	Bulk $\mu\tau$	-0.2 (-13%)	V_{OC}	-0.38 (-41%)
Window Loss	-0.5 (-3%)	ΔE_C	-0.9 (-60%)	R_S	-0.18 (-20%)
Not absorbed	-2.9 (-18%)	SRV	-0.1 (-7%)		
Not collected	-5.3 (-33%)				

necessary. Already, however, a photocurrent of 7.3 mA/cm^2 has been demonstrated in an electrochemically deposited device [27].

Furthermore, the open-circuit voltage potential can be readily addressed by improving the conduction band offset. Finding an n-type material that aligns to within ± 0.3 eV of the Cu_2O conduction band would result in a predicted V_{OC} of 1.2 V. Lastly, in the highest-performing electrochemically deposited Cu_2O cell, fill factor is limited to 0.54 by the low open-circuit voltage. An improvement of V_{OC} to 1.2 V would improve the fill factor to beyond 0.75.

This analysis maps a plausible path to $J_{SC} = 11$ mA/cm^2, $V_{OC} = 1.2$ V, and $FF = 0.75$, by tackling the problems of low bulk $\mu\tau$ and heterojunction ΔE_C first. Together, these innovations would yield a 10% efficiency. This conclusion establishes a very clear set of materials science research priorities, which, if satisfied, could produce a highly efficient Cu_2O device.

5.4 New Structures

Beyond material improvements, alterations to the device structure could benefit efficiency tremendously. These strategies are discussed in the following subsections.

5.4.1 Concentrating in Thinner Cu_2O Layer

Concentrating in a thinner layer, as seen in Section 5.1, can relax the requirements for material quality and allow for high J_{SC} in a thin layer. It can also increase V_{OC} and

FF by separating the quasi-Fermi levels further at higher injection conditions.

The first step to achieving this higher concentration is to texture the front and back surfaces. This already occurs naturally on the front surface during electrochemical deposition, but could be added to the back by anisotropically etching the substrate before or after back contact deposition. The combination of pyramidal texture on the front and back of a thin layer could greatly enhance the optical path length in the material, and allow for efficient collection. Moving to these thinner layers would likely necessitate the use of a p^+ back-surface field to reflect electrons from the back contact, which is possible through nitrogen doping of the Cu_2O.

Improving the concentration depends significantly on reducing front surface reflection and transmission losses. Selecting a window layer material with a low index of refraction near the geometric mean of Cu_2O and air would be a strong first step. Then, selecting the thickness of this layer (or a layer stack) to optimize for destructive interference near the peak of the absorbed spectrum could help transfer more incident photons into the Cu_2O.

The same "cladding" concept of using a low index of refraction material could also be applied to the back surface. For example, using a high work function TCO as the back contact, with a low refractive index, would increase the critical angle for total internal reflection at the back side of the device. A layer stack of low index material on either side of the Cu_2O provides the closest approximation to ideal Yablonovitch light trapping [36]. This possible layer stack is depicted in Fig. 5-9.

5.4.2 Metal-Insulator-Semiconductor (MIS) Structure

One possible replacement for the heterojunction and buffer layer approach would be a variant of the Schottky junction with a thin insulating tunneling layer in between the metal and semiconductor. The thin insulating layer, typically more ionic, will align electronically according to electron affinity rather than charge neutrality level. This allows for the un-pinning of the Fermi level at the semiconductor surface, and a greater degree of tunability for the barrier height. Further, the creation of positive fixed charge (anion vacancies) in the thin insulating layer can improve depletion in

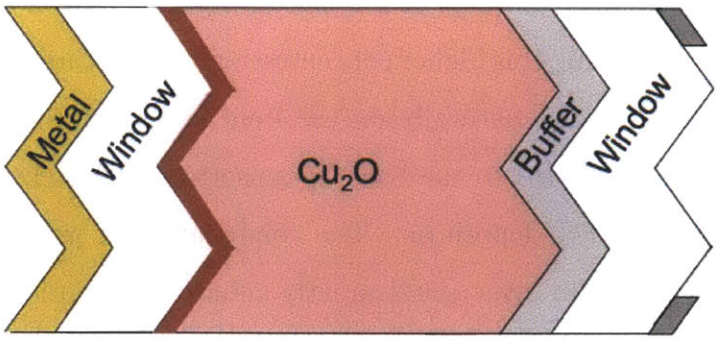

Figure 5-9: A possible layer structure with low index of refraction "cladding" bounding the Cu_2O, in addition to textured surfaces, to trap more photons in a thinner Cu_2O layer. This structure could also include a back surface field with p^+, on the opposite side of illumination, to block electrons and collect holes.

the Cu_2O and lead to a higher built-in potential.

Today, the technology exists with ALD to deposit uniformly thick, conformal tunneling layers of various oxides. Layers $< 2nm$ are necessary to allow for tunneling [60], and can readily be formed by any of the metal oxides listed in Section 5.2. Then, a low work function metal can be evaporated onto the surface, creating an MIS structure. Capping this metal with an inert metal such as Al is common, as low work function metals such as Ca, Mg, and Na tend to be reactive in air. By keeping this metal layer stack very thin (< 10 nm), it is largely transmissive to visible light. However, such a thin layer would have a debilitatingly high sheet resistance. To mitigate this, a TCO may be added on top to reduce the sheet resistance without significantly impacting transmission into the device.

This structure may be modified further by removing the metal entirely, and forming a semiconductor-insulator-semiconductor (SIS) structure [61]. Here, a high carrier concentration TCO acts alone as the Schottky contact, but still with a thin insulating layer separating it from the absorber. A variant of this SIS structure has achieved record thin-film Cu_2O efficiencies of 2.65% [27].

The success of an SIS structure hinges on reducing the electron concentration near the junction, and preventing these electrons from diffusing back into the bulk Cu_2O. It also, as in the MIS structure, can allow for more tunability over the interface and a reduction of the interface state density. Similarly, this can help un-pin the Fermi

level at the interface, allowing for alignment to the Cu_2O more by electron affinity than by charge neutrality level. This may enhance or worsen the conduction band alignment, depending on the specific materials in question.

5.5 Multijunction Cell Modeling

Given the wide bandgap of Cu_2O, the prospect of using it as an eventual top cell in a multijunction device is appealing. It is important, then, to evaluate the critical efficiency thresholds that would enable such a tandem device.

5.5.1 Four-Terminal on Silicon

An obvious choice for a tandem device would be crystalline silicon (c-Si), the predominant material used in the solar industry, with an ideal bottom cell bandgap of 1.1 eV. One way to incorporate a Cu_2O top cell would be as a standalone device, producing power separately from the c-Si. In an ideal case, all photons above 2.0 eV in energy are absorbed in the Cu_2O, with lower energy photons passed to the c-Si. This could be done with a simple stacked layer, or with a prismatic spectral splitter.

Ideally here, the Cu_2O converts the full high-energy spectrum to electricity at a higher voltage than c-Si would , resulting in a higher efficiency than c-Si could offer on its own. However, if the Cu_2O cell "wastes" those photons and converts them to electricity less efficiently than c-Si, the total efficiency may be worse. This is seen in a crossover point in total cell efficiency, in which the bottom cell begins to benefit from the tandem structure. As can be seen in Fig 5.5.1, this crossover point occurs at a different efficiency depending on $E_{g,top}$, and $\eta_{c\text{-}Si}$. For a 2.0 eV top absorber, this transition occurs at efficiencies of 4%, 6%, and 7% for $\eta_{c\text{-}Si}$ = 13%, 17%, and 21% respectively. These are fairly achievable efficiencies, though they would need to be much higher to justify the cost of depositing two cells. Furthermore, the top bandgap of 2.0 eV is suboptimal for a high-performing tandem; $E_{g,top} \approx 1.7$ eV appears to be a better value for achieving high efficiencies.

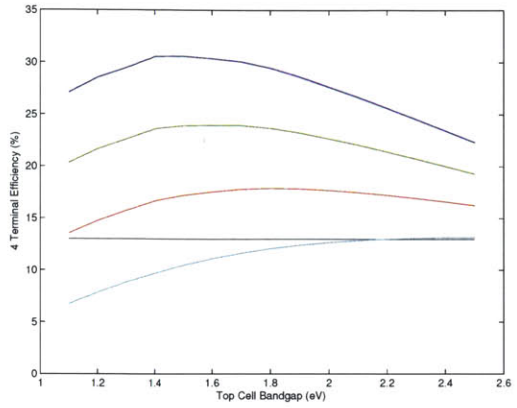

(a) Four terminal tandem with 13% c-Si

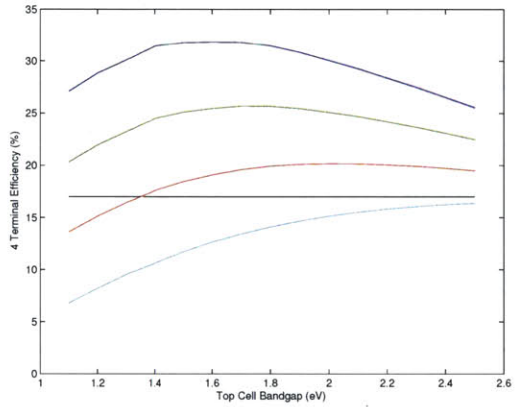

(b) Four terminal tandem with 17% c-Si

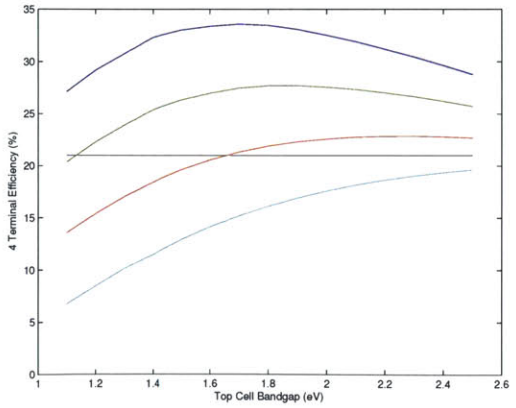

(c) Four terminal tandem with 21% c-Si

Figure 5-10: Efficiency of four terminal multijunctions for different bottom cell efficiencies. The top cell is rated by fraction of its maximum Shockley-Queisser efficiency, (top-blue) 0.8, (green) 0.6, (red) 0.4, and (bottom-turquoise) 0.2. This corresponds to 16%, 12%, 8%, and 4% respectively for the Cu_2O top cell efficiency at 2.0 eV.

5.5.2 Two-Terminal on Silicon

In a two terminal cell, the cost is lower as the bottom cell is used as the substrate, and there is only one power output, minimizing auxiliary materials, power electronics, and capital costs. However, there is a much more stringent requirement of current-matching in these devices, as the device output will be limited by the lowest-current cell. Thus, the window for achieving high efficiencies is significantly reduced.

Efficiency enhancement for a 2.0 eV top cell occurs at an η_{top} of 7%, 10%, and 11%, for $\eta_{c\text{-}Si}$ = 13%, 17%, and 21% respectively. This is in large part due to the difficulty in current-matching 1.1 eV and 2.0 eV absorbers. Turnkey c-Si cells are now exceeding 20% efficiencies, making the prospects of a high-efficiency Cu_2O/Si tandem dimmer. To truly achieve a breakthrough efficiency c-Si tandem, a top cell bandgap in the range of 1.7 eV appears to be the more ideal scenario.

5.5.3 Tandem Devices in CIGS

To overcome the barriers of high efficiency and current matching on c-Si, one alternative would be to form tandem devices on copper indium gallium diselenide (CIGS) solar cells. CIGS has a tunable bandgap from 1.0-1.8 eV, and lower efficiencies overall, potentially allowing for a beneficial tandem. In Fig. 5-12, the efficiencies of various CIGS devices are seen to range from 19% to 9%, largely due to a V_{OC} deficit in high-Ga-content CIGS. Cutting out all photons with energies > 2.0 eV reduces the CIGS efficiency by cutting out photocurrent, but the penalty is not as extreme as it is in c-Si. This is because CIGS cells already forego 50% or more of this short wavelength light, losing it in the ZnO or CdS front layers. Thus, the break-even efficiency threshold for Cu_2O is only 5% for a four-terminal device across the entire bandgap range. A 10% efficient Cu_2O cell could push tandem efficiencies to 25%. However, the same is not true for a two-terminal device. Current-matching constraints again push the threshold Cu_2O efficiency to over 10%.

These simulations make a major simplifying assumption – that all photons with energy > 2.0 eV disappear in the top cell (pessimistic) and that all photons with en-

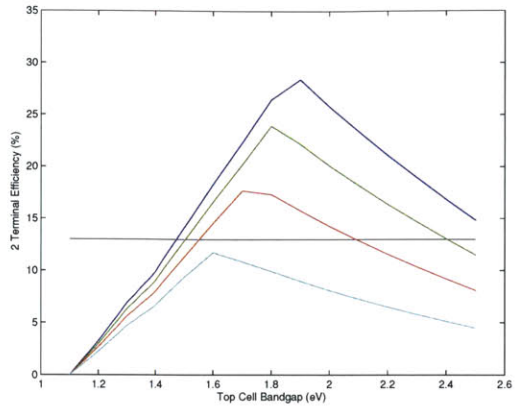

(a) Two terminal tandem with 13% c-Si

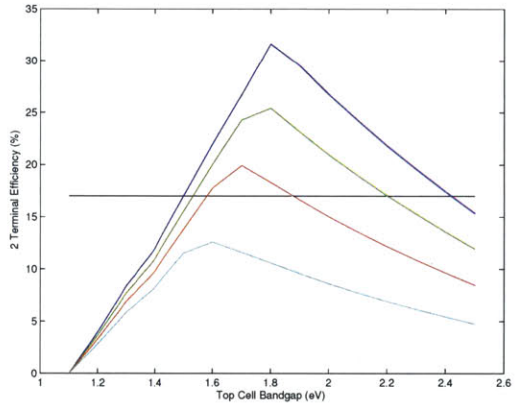

(b) Two terminal tandem with 17% c-Si

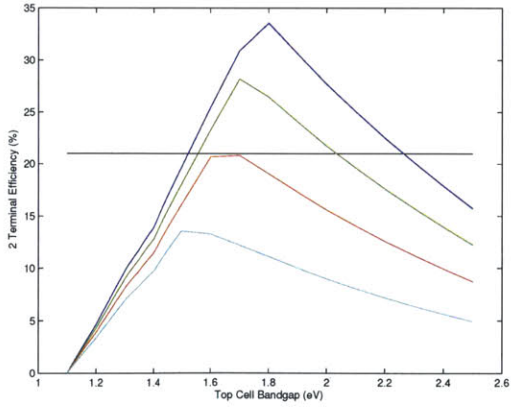

(c) Two terminal tandem with 21% c-Si

Figure 5-11: Efficiency of two terminal multijunctions for different bottom cell efficiencies. The top cell is rated by fraction of its maximum Shockley-Queisser efficiency, (top-blue) 0.8, (green) 0.6, (red) 0.4, and (bottom-turquoise) 0.2. This corresponds to 16%, 12%, 8%, and 4% respectively for the Cu_2O top cell efficiency at 2.0 eV. Current in each cell must match, which puts stricter constraints on bandgap and efficiencies.

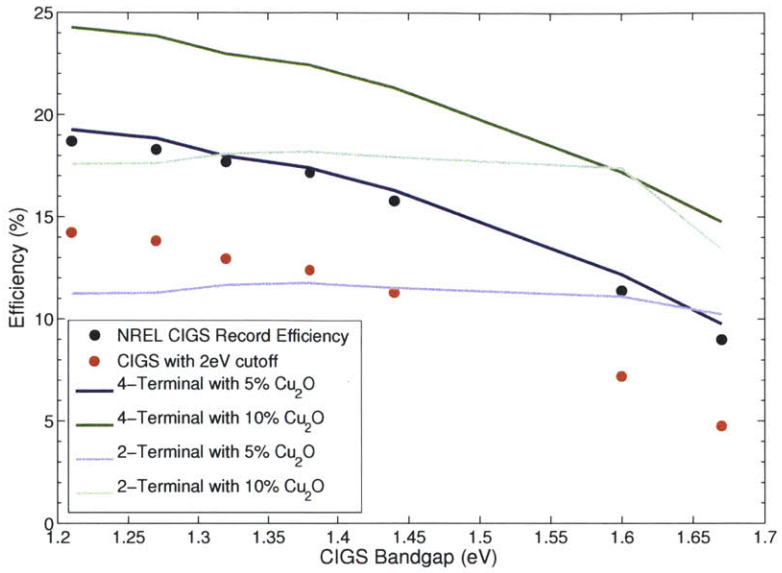

Figure 5-12: Tandem solar cell efficiencies formed with 5% and 10% efficient Cu_2O, on a range of CIGS cells, assuming the record NREL efficiencies for each CIGS bandgap [62].

ergies < 2.0 eV make it through (optimistic). Future simulations of efficiencies should use higher quality optical modeling to predict true illumination spectra and generation profiles. At present, however, the threshold for high efficiency Cu_2O tandems appears to be a very challenging goal in the short-term.

Chapter 6

Conclusions

In summary, cuprous oxide solar cells were fabricated in substrate and superstrate configurations using a variety of layer stacks and thicknesses, as well as processing conditions for each layer. Maximum sputtered superstrate efficiencies of 0.3% and substrate electrodeposited device efficiencies of 0.6% were achieved. This work was performed in parallel with the production of a 2.65% efficient Cu_2O cell in a similar substrate ECD/ALD architecture, which incorporates several learnings from the present work [27]. A suite of characterization and simulation tools was shown to identify the reasons for low efficiencies in Cu_2O solar cells, both in the present work and in literature. In addition to the conventional parasitic optical losses, efficiency losses in Cu_2O devices are largely due to a poor heterojunction band offset, followed by non-radiative recombination in the bulk as well as at the interfaces. This result emphasizes the need for improved n-type materials that can achieve conduction band alignment with Cu_2O, without adversely affecting the interface chemically (by reducing or oxidizing the Cu_2O). If these materials are identified, they may be used in thin buffer layer or thicker transparent conducting applications, depending primarily on their achievable carrier concentration. Long-term, thermal and chemical treatments will be necessary to achieve Cu_2O bulk $\mu\tau$ products in excess of 10^{-7} cm^2/V. Achieving such high quality in a $< 5\mu m$ film will be a critical step for enabling efficiencies $> 10\%$.

However, the prospects for efficient multijunction Cu_2O devices are slim unless

major improvements in the bulk properties (of thin films) are achieved, especially where current-matching is a constraint. Furthermore, the use of Cu_2O as a single junction material is becoming increasingly unlikely as the solar industry's module efficiencies approach and surpass the Shockley-Queisser limit of Cu_2O at 20%. These efficiencies will be necessary to achieve grid parity, as nearly all solar installation costs scale inversely with efficiency. In light of this, it is the hope of the author that Cu_2O may provide further learnings to the thin-film solar community regarding the science of cell operation, but that, more importantly, its lessons may help identify a new material with even greater efficiency potential. With such an efficiency-loss framework in hand, these new materials may be vetted more critically, and may yield quicker improvements in their own performance. This goal of high efficiency in a scalable, single- or multi-junction solar cell, is critical not only to the solar community but to the sustainability and prosperity of the entire world in the coming century.

Appendix A

Full Analytical Solutions to Drift-Diffusion Equations

Poisson's equations with drift and diffusion may be solved numerically or analytically. In many cases, the PV scientist is interested in the built-in potential at the junction, and more specifically, the Fermi level position in the absorber, immediately at the interface. This sets the maximum open-circuit voltage, as it reflects the effective barrier height for holes at the junction.

The derivation of this Fermi level position at the interface, termed $E_{p,a_{z=0}}$, has been performed by previous authors, and is reproduced here from derivations by Unold and Schock [63].

The built-in potential of a homojunction is merely the electrochemical potential difference between the n and p type layers, and can be simplified if the doping densities in each layer are known:

$$qV_{\mathrm{bi}} = E_{\mathrm{f},n} - E_{\mathrm{f},p} = k_B T log(\frac{N_{\mathrm{A}} N_{\mathrm{D}}}{n_{\mathrm{i}}^2}). \tag{A.1}$$

If there is instead a band offset between the two layers, as in a heterojunction, the built-in potential can be defined by the conduction band offset ΔE_{C}, and the Fermi level positions within the absorber $E_{p,a}$ and window $E_{n,w}$, referenced to the valence

band and conduction bands respectively.

$$qV_{\mathrm{bi}} = E_{\mathrm{g,a}} - E_{\mathrm{n,w}} - E_{\mathrm{p,a}} + \Delta E_{\mathrm{C}} \tag{A.2}$$

For a simple p-n^+, heterojunction, in which most of the depletion region occurs in the absorber layer, the p-layer potential drop is:

$$V_{\mathrm{jp}} = (V_{\mathrm{bi}} - V_{\mathrm{A}})\Big(\frac{\varepsilon_{\mathrm{w}} N_{\mathrm{D,w}}}{\varepsilon_{\mathrm{w}} N_{\mathrm{D,w}} + \varepsilon_{\mathrm{a}} N_{\mathrm{A,a}}}\Big). \tag{A.3}$$

Here, V_{A} is the applied voltage across the junction, which opposes the built-in potential. In addition, the depletion depth in the p-type absorber layer is:

$$W_{\mathrm{a}} = \Big(\frac{2\varepsilon_{\mathrm{a}} V_{\mathrm{jp}}}{qN_{\mathrm{A,a}}}\Big)^{1/2}. \tag{A.4}$$

For simplicity, we define the quantity $\Omega = \varepsilon_{\mathrm{a}} N_{\mathrm{A,a}} + \varepsilon_{\mathrm{w}} N_{\mathrm{D,w}}$. Knowing the potential drop and depletion depth, the electric potential in the depletion region is parabolic:

$$V(x) = \frac{qN_{\mathrm{A,a}}}{2\varepsilon_{\mathrm{a}}}(x + W_a)^2, \quad \text{for} - W_a < x < 0. \tag{A.5}$$

Now, the Fermi level at the interface will be the sum of the Fermi level in the bulk plus the potential drop borne by the p-type absorber. This reflects where the Fermi level is pinned at the interface, which will set the open-circuit voltage.

$$E_{\mathrm{p,a}_{z=0}} = E_{\mathrm{p,a}} + qV_{\mathrm{jp}}. \tag{A.6}$$

Now, we can consider the possibility of there being interfacial charge N_{IF} between the absorber and window, which changes the conditions for charge neutrality across the junction:

$$-qN_{\mathrm{A,a}} W_{\mathrm{a}} + zqN_{\mathrm{IF}} + qN_{\mathrm{D,w}} W_{\mathrm{w}} = 0 \tag{A.7}$$

where z = $\pm$ 1 for positive or negative interface charge. This is true only if the absorber is not depleted all the way to the back contact, in which case charge transfer from

the contact must be considered. Poisson's equation may be re-solved for this new neutrality condition, to give a new built-in barrier height in the absorber:

$$E_{\mathrm{p,a}_{z=0}} = E_{\mathrm{p,a}} + \frac{q\varepsilon_{\mathrm{w}}N_{\mathrm{D,w}}}{\Omega}(V_{\mathrm{bi}} - V_{\mathrm{A}}) - \frac{qN_{\mathrm{IF}}^2}{2\Omega^2}(\varepsilon_{\mathrm{w}}N_{\mathrm{D,w}} - \varepsilon_{\mathrm{a}}N_{\mathrm{A,a}}) + \frac{zqN_{\mathrm{IF}}}{\Omega^2}\sqrt{\varepsilon_{\mathrm{w}}N_{\mathrm{D,w}} - \varepsilon_{\mathrm{a}}N_{\mathrm{A,a}}\left(\frac{2\Omega}{q}(V_{\mathrm{bi}} - V_{\mathrm{A}}) - N_{\mathrm{IF}}^2\right)} \quad \text{(A.8)}$$

The depletion depth is now:

$$W_{\mathrm{a}} = \frac{z\varepsilon_{\mathrm{a}}N_{\mathrm{IF}}}{\Omega} + \sqrt{\frac{\varepsilon_{\mathrm{a}}\varepsilon_{\mathrm{w}}N_{\mathrm{D,w}}[\frac{2\Omega}{q}(V_{\mathrm{bi}} - V_{\mathrm{A}}) - N_{\mathrm{IF}}^2]}{N_{\mathrm{A,a}}\Omega^2}} \quad \text{(A.9)}$$

These two equations reduce to equations A.3 and A.4 when interfacial charge goes to zero. For positive interface fixed charge, the barrier height increases, while for negative fixed charge the barrier, and inversion layer, can disappear. However, a highly doped window layer can reduce the influence of the interface charge by screening.

Another simple alteration is the inclusion of a thin buffer layer of n type conductivity between the absorber and window, with its own depletion depth and donor density $N_{\mathrm{D,b}}$. Now, the equation for charge neutrality becomes:

$$-qN_{\mathrm{A,a}}W_{\mathrm{a}} + qN_{\mathrm{D,b}}W_{\mathrm{b}} + qN_{\mathrm{D,w}}W_{\mathrm{w}} = 0. \quad \text{(A.10)}$$

The buffer layer is presumed to be depleted such that W_{b} is the full buffer layer thickness d_{b}. In the case of zero interface charge, this results in an interfacial Fermi level energy of:

$$E_{\mathrm{p,a}_{z=0}} = q(V_{\mathrm{bi}} - V_{\mathrm{A}}) + E_{\mathrm{p,a}} + \frac{q^2N_{\mathrm{D,b}}d_{\mathrm{b}}}{2\varepsilon_{\mathrm{b}}} - \frac{q^2N_{\mathrm{A,a}}d_{\mathrm{b}}}{\varepsilon_{\mathrm{b}}}W_{\mathrm{a}}, \quad \text{(A.11)}$$

where:

$$qV_{\mathrm{bi}} = E_{\mathrm{g,a}} - E_{\mathrm{n,w}} - E_{\mathrm{p,a}} + \Delta E_{\mathrm{C}}^{\mathrm{w,b}} + \Delta E_{\mathrm{C}}^{\mathrm{b,a}}. \quad \text{(A.12)}$$

The built-in potential must be solved simultaneously with the depletion depth:

$$W_{\mathrm{a}} = -\frac{\varepsilon_{\mathrm{a}} d_{\mathrm{b}}}{\varepsilon_{\mathrm{b}}} + \sqrt{\left(\frac{\varepsilon_{\mathrm{a}} d_{\mathrm{b}}}{\varepsilon_{\mathrm{b}}}\right)^2 + \frac{2\varepsilon_{\mathrm{a}}}{q^2 N_{\mathrm{A,a}}}\left(q(V_{\mathrm{bi}} - V_{\mathrm{A}}) + \frac{q^2 N_{\mathrm{D,b}} d_{\mathrm{b}}^2}{2\varepsilon_{\mathrm{b}}}\right)}. \tag{A.13}$$

As one can see, the equations for mere band alignment become more and more difficult to solve analytically. Now, if interfacial charge is added, the charge neutrality conditions must be combined. Furthermore, if the interfacial charge is caused by the filling of defect levels, it becomes Fermi-level dependent as well. These intertwined effects can only be solved numerically.

This series of equations shows several ways in which Poisson's equations may be reduced to analytical expressions. However, to perform true device simulations, it is clear that numerical simulation is necessary. With the equations for charge neutrality, drift and diffusion transport, and continuity, any device stack may theoretically be simulated.

A final section which is not well treated in the present system of equations is tunneling. Here, charge transport may occur by tunneling between defect levels or across thin potential barriers. This phenomenon becomes very important for tunneling ohmic contacts, and for the operation of SIS and MIS structures as well as any heterojunction with defective interfaces. Real device simulations must take this into account.

Bibliography

[1] OY Not Solar. World solar insolation map. Website, December 2009. http://oynot.com.p12.hostingprod.com/solar-insolation-map.html.

[2] Paula Mints. 2012 Solar Manufacturers Report. Navigant Consulting, April 2013.

[3] Alexandre-Edmond Becquerel. Mémoire sur les effets électriques produits sous l'influence des rayons solaires. *Comptes Rendus*, 9(567):1839, 1839.

[4] A. H. Pfund. The light sensitiveness of copper oxide. *Physical Review*, 7(3):289–301, 1916.

[5] Allen D. Garrison. The behavior of cuprous oxide photovoltaic cells. *Journal of Physical Chemistry*, 27(7):601–622, 1923.

[6] L. O. Grondahl. Theories of a new solid junction rectifier. *Science*, 64(1656):306–308, 1926.

[7] Yun Seog Lee, Mark T Winkler, Sin Cheng Siah, Riley Brandt, and Tonio Buonassisi. Hall mobility of cuprous oxide thin films deposited by reactive direct-current magnetron sputtering. *Applied Physics Letters*, 98(19):192115–192115, 2011.

[8] Hannes Raebiger, Stephan Lany, and Alex Zunger. Origins of the p-type nature and cation deficiency in Cu_2O and related materials. *Physical Review B*, 76(4):045209, 2007.

[9] A. E. Rakhshani. Preparation, characteristics and photovoltaic properties of cuprous oxide: A review. *Solid-State Electronics*, 29(1):7–17, 1986.

[10] Leonidas Papadimitriou, Nicolaos A Economou, and Dan Trivich. Heterojunction solar cells on cuprous oxide. *Solar Cells*, 3(1):73–80, 1981.

[11] Alberto Mittiga, Enrico Salza, Francesca Sarto, Mario Tucci, and Rajaraman Vasanthi. Heterojunction solar cell with 2% efficiency based on a Cu_2O substrate. *Applied Physics Letters*, 88(16):163502–163502, 2006.

[12] Tadatsugu Minami, Yuki Nishi, Toshihiro Miyata, and Jun-ichi Nomoto. High-efficiency oxide solar cells with ZnO/Cu_2O heterojunction fabricated on thermally oxidized Cu_2O sheets. *Applied Physics Express*, 4(6):2301, 2011.

[13] Yuki Nishi, Toshihiro Miyata, and Tadatsugu Minami. Effect of inserting a thin buffer layer on the efficiency in n-ZnO/p-Cu_2O heterojunction solar cells. *Journal of Vacuum Science & Technology A: Vacuum, Surfaces, and Films*, 30(4):04D103–04D103, 2012.

[14] Tadagatsu Minami, Yuki Nishi, Toshihiro Miyata, and Shinya Abe. Photovoltaic properties in Al-doped ZnO/non-doped $Zn_{1-x}Mg_xo/Cu_2O$ heterojunction solar cells. *ECS Meeting Abstracts*, MA2012-02(38):2886, 2012.

[15] Chengxiang Xiang, Gregory M Kimball, Ronald L Grimm, Bruce S Brunschwig, Harry A Atwater, and Nathan S Lewis. 820 mV open-circuit voltages from Cu_2O/CH_3CN junctions. *Energy & Environmental Science*, 4(4):1311–1318, 2011.

[16] B. K. Meyer, A. Polity, D. Reppin, M. Becker, P. Hering, P. J. Klar, T. Sander, C. Reindl, J. Benz, and M. Eickhoff. Binary copper oxide semiconductors: From materials towards devices. *Physica Status Solidi (b)*, 249(8):1487–1509, 2012.

[17] G K Paul, R Ghosh, S K Bera, S Bandyopadhyay, T Sakurai, and K Akimoto. Deep level transient spectroscopy of cyanide treated polycrystalline p-Cu_2O/n-ZnO solar cell. *Chemical Physics Letters*, 463(1):117–120, 2008.

[18] Jhin-Wei Chen, Dung-Ching Perng, and Jia-Feng Fang. Nano-structured Cu_2O solar cells fabricated on sparse ZnO nanorods. *Solar Energy Materials and Solar Cells*, 95(8):2471–2477, 2011.

[19] T Unold and H W Schock. Nonconventional (non-silicon-based) photovoltaic materials. *Annual Review of Materials Research*, 41:297–321, 2011.

[20] Paul A Basore. Numerical modeling of textured silicon solar cells using PC-1D. *IEEE Transactions on Electron Devices*, 37(2):337–343, 1990.

[21] Hong Zhu, Ali Kaan Kalkan, Jingya Hou, and Stephen J Fonash. Applications of AMPS-1D for solar cell simulation. In *AIP Conference Proceedings*, volume 462, page 309, 1999.

[22] R Stangl, M Kriegel, and M Schmidt. AFORS-HET, version 2.2, a numerical computer program for simulation of heterojunction solar cells and measurements. In *Conference Record of the 2006 IEEE 4th World Conference on Photovoltaic Energy Conversion*, volume 2, pages 1350–1353. IEEE, 2006.

[23] A. Niemegeers, M. Burgelman, R. Herberholz, U. Rau, D. Hariskos, and H.W. Schock. Model for electronic transport in Cu(In,Ga)Se_2 solar cells. *Progress in Photovoltaics: Research and Applications*, 6(6):407–421, 1998.

[24] Marc Burgelman, Peter Nollet, and Stefaan Degrave. Modelling polycrystalline semiconductor solar cells. *Thin Solid Films*, 361:527–532, 2000.

[25] Claudia Malerba, Francesco Biccari, Cristy Leonor Azanza Ricardo, Mirco D'Incau, Paolo Scardi, and Alberto Mittiga. Absorption coefficient of bulk and thin film Cu_2O. *Solar Energy Materials and Solar Cells*, 95(10):2848–2854, 2011.

[26] SOPRA. Optical constants of Cu_2O (copper(I) oxide, cuprite). Sopra n and k Database, December 2012. http://refractiveindex.info/.

[27] Yun Seog Lee, Jaeyeong Heo, Sin Cheng Siah, Jonathan Mailoa, Riley Brandt, Sang Bok Kim, Roy Gordon, and Tonio Buonassisi. Ultrathin amorphous zinc-tin-oxide buffer layer for enhancing heterojunction interface quality in metal-oxide solar cells. *Energy Environ. Sci., DOI:10.1039/C3EE24461J*, 2013.

[28] Armin Richter, Stefan W Glunz, Florian Werner, Jan Schmidt, and Andres Cuevas. Improved quantitative description of Auger recombination in crystalline silicon. *Physical Review B*, 86(16):165202, 2012.

[29] Kotaro Mizuno, Masanobu Izaki, Kuniaki Murase, Tsutomu Shinagawa, Masaya Chigane, Minoru Inaba, Akimasa Tasaka, and Yasuhiro Awakura. Structural and electrical characterizations of electrodeposited p-type semiconductor Cu_2O films. *Journal of The Electrochemical Society*, 152(4):C179–C182, 2005.

[30] Francesco Biccari. *Defects and Doping in Cu_2O.* PhD thesis, Universita di Roma, 2009.

[31] D K Zhang, Y C Liu, Y L Liu, and H Yang. The electrical properties and the interfaces of Cu_2O/ZnO/ITO p-i-n heterojunction. *Physica B: Condensed Matter*, 351(1):178–183, 2004.

[32] David O Scanlon, Benjamin J Morgan, Graeme W Watson, and Aron Walsh. Acceptor levels in p-type Cu_2O: Rationalizing theory and experiment. *Physical review letters*, 103(9):096405, 2009.

[33] Dahlang Tahir and Sven Tougaard. Electronic and optical properties of Cu, CuO and Cu_2O studied by electron spectroscopy. *Journal of Physics: Condensed Matter*, 24(17):175002, 2012.

[34] D DeNardis, D Rosales-Yeomans, L Borucki, and A Philipossian. Studying the effect of temperature on the copper oxidation process using hydrogen peroxide for use in multi-step chemical mechanical planarization models. *Thin Solid Films*, 518(14):3903–3909, 2010.

[35] Steven S Hegedus and William N Shafarman. Thin-film solar cells: Device measurements and analysis. *Progress in Photovoltaics: Research and Applications*, 12(2-3):155–176, 2004.

[36] Eli Yablonovitch. Inhibited spontaneous emission in solid-state physics and electronics. *Physical Review Letters*, 58(20):2059–2062, 1987.

[37] S Ishizuka, S Kato, Y Okamoto, and K Akimoto. Hydrogen treatment for polycrystalline nitrogen-doped Cu_2O thin film. *Journal of Crystal Growth*, 237:616–620, 2002.

[38] S Ishizuka, S Kato, Y Okamoto, T Sakurai, K Akimoto, N Fujiwara, and H Kobayashi. Passivation of defects in polycrystalline Cu_2O thin films by hydrogen or cyanide treatment. *Applied Surface Science*, 216(1):94–97, 2003.

[39] W A Jesser and J W Matthews. Growth of copper, silver, and gold on twelve alkali halides cleaved in vacuum. *Journal of Crystal Growth*, 5(2):83–89, 1969.

[40] Walter Schottky. Halbleitertheorie der sperrschicht. *Naturwissenschaften*, 26(52):843–843, 1938.

[41] John Bardeen. Surface states and rectification at a metal semi-conductor contact. *Physical Review*, 71(10):717, 1947.

[42] Volker Heine. Theory of surface states. *Physical Review*, 138(6A):A1689, 1965.

[43] Hideki Hasegawa and Hideo Ohno. Unified disorder induced gap state model for insulator–semiconductor and metal–semiconductor interfaces. *Journal of Vacuum Science & Technology B: Microelectronics and Nanometer Structures*, 4(4):1130–1138, 1986.

[44] J Tersoff. Band lineups at II-VI heterojunctions: Failure of the common-anion rule. *Physical Review Letters*, 56(25):2755–2758, 1986.

[45] J Robertson and SJ Clark. Limits to doping in oxides. *Physical Review B*, 83(7):075205, 2011.

[46] David R. Lide. *CRC Handbook of Chemistry and Physics*, volume 1 of *CRC Handbook of Chemistry and Physics*, section 1, pages 12–114. CRC Press, United States, 89th edition, 17 June 2008.

[47] L. C. Olsen, R. C. Bohara, and M. W. Urie. Explanation for low-efficiency Cu_2O Schottky-barrier solar cells. *Applied Physics Letters*, 34:47–49, 1979.

[48] John Robertson. Band offsets of wide-band-gap oxides and implications for future electronic devices. *Journal of Vacuum Science & Technology B: Microelectronics and Nanometer Structures*, 18(3):1785–1791, 2000.

[49] J Robertson and B Falabretti. Band offsets of high k gate oxides on III-V semiconductors. *Journal of Applied Physics*, 100(1):014111–014111, 2006.

[50] John Robertson. Electronic structure and band offsets of high-dielectric-constant gate oxides. *MRS Bulletin*, 27(03):217–221, 2002.

[51] Lei Huang, Feng Peng, and Fumio S Ohuchi. *In-situ* XPS study of band structures at Cu_2O/TiO_2 heterojunction interface. *Surface Science*, 603(17):2825–2834, 2009.

[52] B Kramm, A Laufer, D Reppin, A Kronenberger, P Hering, A Polity, and B K Meyer. The band alignment of Cu_2O/ZnO and Cu_2O/GaN heterostructures. *Applied Physics Letters*, 100(9):094102–094102, 2012.

[53] C J Dong, W X Yu, M Xu, J J Cao, C Chen, W W Yu, and Y D Wang. Valence band offset of Cu_2O/In_2O_3 heterojunction determined by X-ray photoelectron spectroscopy. *Journal of Applied Physics*, 110(7):073712–073712, 2011.

[54] Jonas Deuermeier, Jurgen Gassmann, Joachim Brotz, and Andreas Klein. Reactive magnetron sputtering of Cu_2O: Dependence on oxygen pressure and interface formation with indium tin oxide. *Journal of Applied Physics*, 109(11):113704–113704, 2011.

[55] S Y Yang, J Seidel, S J Byrnes, P Shafer, C-H Yang, M D Rossell, P Yu, Y-H Chu, J F Scott, J W Ager, et al. Above-bandgap voltages from ferroelectric photovoltaic devices. *Nature Nanotechnology*, 5(2):143–147, 2010.

[56] Yi Ke, Joseph Berry, Philip Parilla, Andriy Zakutayev, Ryan O'Hayre, and David Ginley. The origin of electrical property deterioration with increasing Mg concentration in ZnMgO: Ga. *Thin Solid Films*, 520(9):3697–3702, 2012.

[57] Shigeki Yamaga, Akihiko Yoshikawa, and Haruo Kasai. Growth and properties of iodine-doped ZnS films grown by low-pressure MOCVD using ethyliodine as a dopant source. *Journal of Crystal Growth*, 106(4):683–689, 1990.

[58] Fusen Chen and Ling Chen. Atomically thin highly resistive barrier layer in a copper via, February 23 2001. US Patent App. 09/792,737.

[59] Allen Rothwarf. Photovoltaics in heterojunctions: Particularly CdS/Cu_2S. In *International Conference on CdS/Cu_2S Solar Cells*, 1975.

[60] Martin A Green and RB Godfrey. MIS solar cell: General theory and new experimental results for silicon. *Applied Physics Letters*, 29(9):610–612, 1976.

[61] J Shewchun, J Dubow, A Myszkowski, and R Singh. The operation of the semiconductor-insulator-semiconductor (SIS) solar cell: Theory. *Journal of Applied Physics*, 49(2):855–864, 1978.

[62] M. Contreras, L. Mansfield, B. Egaas, J. Li, M. Romero, and R. Noufi. Improved energy conversion efficiency in wide-bandgap Cu(In,Ga)Se_2 solar cells. In *Proc. 37th IEEE Photovoltaic Specialists Conference (PVSC 37)*, 2011.

[63] Roland Scheer and Hans-Werner Schock. *Chalcogenide Photovoltaics: Physics, Technologies, and Thin Film Devices*, volume 1 of *Wiley*, chapter 2, pages 9–122. Wiley-VCH, Weinheim, Germany, first edition, 2011.